Geophys. J. Int. (2009) **176,** 63–80 doi: 10.1111/j.1365-246X.2008.03950.x

2.5-D/3-D resistivity modelling in anisotropic media using Gaussian quadrature grids

Bing Zhou,[1] Mark Greenhalgh[1] and S. A. Greenhalgh[1,2]

[1]*Department of Physics, Adelaide University, North Terrace, SA* 5005, *Australia. E-mail: bing.zhou@adelaide.edu.au*
[2]*Institute of Geophysics, ETH Zürich,* 8093 *Hönggerberg, Switzerland*

Accepted 2008 August 22. Received 2008 July 16; in original form 2008 March 24

SUMMARY

We present a new numerical scheme for 2.5-D/3-D direct current resistivity modelling in heterogeneous, anisotropic media. This method, named the 'Gaussian quadrature grid' (GQG) method, cooperatively combines the solution of the Variational Principle of the partial differential equation, Gaussian quadrature abscissae and local cardinal functions so that it has the main advantages of the spectral element method. The formulation shows that the GQG method is a modification of the spectral element method but does not employ the constant elements or require the mesh generator to match the Earth's surface. This makes it much easier to deal with geological models having a 2-D/3-D complex topography than using traditional numerical methods. The GQG technique can achieve a similar convergence rate to the spectral element method. We show it transforms the 2.5-D/3-D resistivity modelling problem into a sparse and symmetric linear equation system that can be solved by an iterative or matrix inversion method.

Comparison with analytic solutions for homogeneous isotropic and anisotropic models shows that the error depends on the Gaussian quadrature order (abscissa number) and the subdomain size. The higher the order or the smaller the subdomain size that is employed, the more accurate are the results obtained. Several other synthetic examples, both homogeneous and inhomogeneous, incorporating sloping, undulating and severe topography, are presented and found to yield results comparable to finite element solutions involving a dense mesh.

Key words: Numerical solutions; Electrical properties; Electromagnetic theory.

INTRODUCTION

For electrical resistivity modelling, two numerical methods are commonly employed. One is the finite difference method (FDM) and the other is the finite element method (FEM), both of which are used to solve the governing partial differential equation (Poisson equation or Helmholtz equation), which describes the electric potential in a heterogeneous medium (see Section Variational Principle). The FDM applies difference operators to approximate the vector calculus gradient and divergence operators in the governing equation (Mufti 1976; Dey & Morrison 1979a, 1979b; Mundry 1984; James 1985; Spitzer 1995), whereas the FEM converts the partial differential equations into integral equations by a Variational Principle or Galerkin method, then carries out a numerical integration (Coggon 1971; Fox *et al.* 1980; Pridmore *et al.* 1981; Holcombe & Jirack 1984; Querlat *et al.* 1991; Zhou & Greenhalgh 2001). To overcome the numerical problems at the source and limitations of the artificial boundary conditions (combined Neumann and Dirichelet condition, see Dey & Morrison 1979a, b) under the Earth, singularity removal techniques (Lowry *et al.* 1989; Zhao & Yedlin 1996) and infinite element methods (Blome & Maurer 2007) have been developed. However, few researchers have incorporated anisotropy into the modelling (Yin & Weidelt 1999; Pain *et al.* 2003; Li & Spitzer 2005; Pervago *et al.* 2006), even though it is often very important when dealing with layered, fractured or cleaved rocks and can lead to large errors in interpretation, if ignored (Habberjam 1972; Asten 1974).

In many applications of 2.5-D or 3-D resistivity imaging, we often encounter a geological model that has a complex topography, such as small cliffs, steep hills and large trenches. Such natural conditions pose a difficulty for numerical modelling with the FDM. The boundary element methods (Lee 1975; Das & Parasnis 1987; Eskola 1992; Hvodara & Kaikkonene 1998) deal well with such situations, but they tend to be restricted to simple models entailing embedded bodies in an otherwise homogeneous or layered half-space. Most researchers prefer the FEM in which some 2-D/3-D grid generators in computer graphics, such as TetGen (3-D) and Delaunay Traingulator (2-D), are applied to the finite element mesh that fits the complex topography (Loke 2000; Shewchuk 2002; Rücker *et al.* 2006; Kerry & Weiss 2006). However, employing such grid generators, one hardly knows in advance where the grid nodes are located and it results in an irregular parametrization

for forward modelling and inversion. We sought to develop a new numerical method that can handle a complex topography without the grid generator and can control the node distribution or model parametrization in forward modelling and inversion. Furthermore, we wanted to be able to include anisotropy in the model.

It has been shown that the spectral method (Trefethen 2000) and the spectral element method (Komatitsch & Tromp 1999) have more attractive features than the two traditional FDM and FEM numerical methods. The main advantages lie in the capability to simulate complex physical models and the exponential power convergence. They have been successfully applied to fluid-flow dynamic modelling (Boyd 1989), seismic wave simulations (Komatitsch & Tromp 1999) and electromagnetic computations (Martinec 1999). The spectral method uses some global series of orthogonal functions to represent the unknown solution at the irregular collocation points, subject to the boundary condition, and achieves a convergence rate of exponential power. However, it gives rise to a fully occupied system matrix. The spectral element method combines the spectral method and the finite element method, and it possesses the main advantages of each, such as capability for various model shapes, the sparse matrix structure of the FEM and the exponential power convergence of the spectral method.

In this paper, we develop a new numerical method for 2.5-D/3-D DC resistivity modelling in heterogeneous, anisotropic media, having arbitrary surface topography. The method differs from the spectral method, but it retains all the main advantages of the advanced numerical method. This method, referred to as the Gaussian Quadrature Grid (GQG) method, is a modified version of the spectral element method in which we discretize the model domain with the Gaussian quadrature abscissae rather than constant elements, then employ local cardinal functions to calculate the unknown potential values and their gradients at the abscissae, which leads to a sparse and symmetric linear equation system. The main features of the method are no requirement for a constant-element mesh matching the surface topography, so that it avoids employing a 2-D/3-D mesh generator and enables us to control the model parametrization and makes complex forward modelling much easier.

VARIATIONAL PRINCIPLE

The Variational Principle is the basis of our method. For completeness, we give a brief introduction here. More details can be found in the book by Graham & Oden (1983, p. 96). The Variational Principle states that the following boundary-value problem of a partial differential equation

$$\begin{cases} Du = f, & r \in \Omega, \\ \frac{\partial u}{\partial n} + \nu u = 0, & r \in \Gamma, \end{cases} \tag{1}$$

may be solved by minimizing the following functional

$$\Psi(u) = \frac{1}{2}\langle u, Du\rangle - \langle u, f\rangle, \tag{2}$$

incorporating the boundary condition, provided the differential operator D is positive, linear and self-adjoint. This means that the following equations are satisfied for arbitrary differentiable functions u, v, w and a constant λ.

$$\begin{aligned} &\langle u, Du\rangle > 0, \\ &\langle w, Du\rangle = \langle u, Dw\rangle, \\ &\langle w, D(u+\lambda v)\rangle = \langle w, Du\rangle + \lambda\langle w, Dv\rangle. \end{aligned} \tag{3}$$

Here, the angular bracket stands for the integral over the domain Ω:

$$\langle f, g\rangle = \int_\Omega f(r)g(r)\mathrm{d}\Omega. \tag{4}$$

The principle is based on the variational analysis for an arbitrary small change δu, which gives rise to

$$\begin{aligned} \delta\Psi &= \frac{1}{2}[\langle \delta u, Du\rangle + \langle u, D\delta u\rangle] - \langle \delta u, f\rangle \\ &= \frac{1}{2}[\langle \delta u, Du\rangle + \langle \delta u, Du\rangle] - \langle \delta u, f\rangle \\ &= \langle \delta u, Du - f\rangle = 0. \end{aligned} \tag{5}$$

Eq. (5) shows that $\delta\Psi$ vanishes if and only if $Du = f$, $\forall\delta u$, which is the governing equation in the boundary-valued problem (1).

RESISTIVITY MODELLING—BASIC EQUATIONS

The Variational Principle may be applied to 2.5-D and 3-D resistivity anisotropic forward modelling in which the governing equations are

$$\text{2.5-D}: \begin{cases} \nabla\cdot(\boldsymbol{\sigma}\cdot\nabla\tilde{G}) + k_y^2\boldsymbol{\sigma}_{yy}\tilde{G} = -\frac{1}{2}\delta(r - r_s), & r = (x, z) \in \Omega, \\ (\boldsymbol{\sigma}\cdot\nabla\tilde{G})\cdot\mathbf{n} + \nu\tilde{G} = 0, & r = (x, z) \in \Gamma, \end{cases} \tag{6}$$

$$\text{3-D}: \begin{cases} \nabla \cdot (\boldsymbol{\sigma} \cdot \nabla G) = -\delta(r - r_s), \quad r = (x, y, z) \in \Omega, \\ (\boldsymbol{\sigma} \cdot \nabla G) \cdot \mathbf{n} + \nu G = 0, \quad r = (x, y, z) \in \Gamma. \end{cases} \tag{7}$$

Here $\boldsymbol{\sigma}$ is in general a 2×2 or 3×3 symmetric conductivity matrix in the 2.5-D or 3-D case, $\mathbf{n}$ is the unit normal vector to the boundary Γ, ν is a known function of the spatial coordinates and the conductivity and specifies the mixed boundary condition (see Appendix A), r_s is the current point-source location, and $\tilde{G}$ or G is the Green's function (the potential response to a unit current injection) in the wavenumber (Fourier transformed wrt the strike or y direction) or spatial domain, respectively. If the medium has elliptical anisotropy, that is, defined by the three principal values ($\sigma_{x'x'}$, $\sigma_{y'y'}$, $\sigma_{z'z'}$) and with the symmetry-axis in the $\hat{\mathbf{z}}$ direction defined by the orientation angles (φ_0, θ_0), the conductivity tensor $\boldsymbol{\sigma}$ has components (see Appendix B, eqs B4 and B3)

$$\boldsymbol{\sigma} = \begin{pmatrix} \sigma_{xx} & \sigma_{xz} \\ \sigma_{xz} & \sigma_{zz} \end{pmatrix} \tag{8a}$$

in the 2.5-D case, and

$$\boldsymbol{\sigma} = \begin{pmatrix} \sigma_{xx} & \sigma_{xy} & \sigma_{xz} \\ \sigma_{xy} & \sigma_{yy} & \sigma_{yz} \\ \sigma_{xz} & \sigma_{yz} & \sigma_{zz} \end{pmatrix} \tag{8b}$$

in the 3-D case. Therefore, we have the functional

$$\Psi(\tilde{G}) = \frac{1}{2} \left\{ \int_\Omega [(\sigma \cdot \nabla \tilde{G}) \cdot \nabla \tilde{G} + k_y^2 \sigma_{yy} \tilde{G}^2] \mathrm{d}\Omega + \int_\Gamma \nu \tilde{G}^2 \mathrm{d}\Gamma - \tilde{G}_s \right\} \tag{9}$$

and

$$\Psi(G) = \frac{1}{2} \int_\Omega [(\sigma \cdot \nabla G) \cdot \nabla G] d\Omega + \frac{1}{2} \int_\Gamma \nu G^2 d\Gamma - G_s \tag{10}$$

for 2.5-D and 3-D modelling, respectively. Here, $\tilde{G}_s$or G_s means the value of the Green's function at the source position, which may be expressed by the interpolation formula of the neighbouring points (see the Section Discretization of a 2-D Functional).

DISCRETIZATION OF A 2-D FUNCTIONAL

For 2.5-D resistivity modelling, the subsurface is often limited by a 2-D computational domain, i.e $(x, z) \in [x_1, x_{N_x}] \times [0, z_0(x)]$, where the function $z_0(x)$ gives the topography of the Earth's surface (see Fig. 1). The functional given in the previous section may be calculated by summation of successive integrals over the intervals L_i: $[x_i, x_{i+1}]$, $(i = 1, 2, \ldots, N_x - 1; N_x \geq 2)$ in which the topography $z_0(x)$ is piecewise differentiable, that is, $z_0(x) \in C^1(L_i)$, the integral becomes

$$\int_\Omega F(\sigma, \tilde{G}, \nabla \tilde{G}) \mathrm{d}\Omega = \sum_{\mathrm{i}=1}^{\mathrm{N_x}-1} \left[\int_{\mathrm{x_i}}^{\mathrm{x_{i+1}}} \int_0^{\mathrm{z_0(x)}} \mathrm{F}(\sigma, \tilde{\mathrm{G}}, \nabla \tilde{\mathrm{G}}) \mathrm{d}x \mathrm{d}z \right], \tag{11}$$

where the integrand $F(\sigma, \tilde{G}, \nabla \tilde{G})$ is a function of the conductivity tensor $\boldsymbol{\sigma}$, the field quantity $\tilde{G}$ and its gradient $\nabla \tilde{G}$, all of which, in general, vary with the spatial coordinates $(x, z) \in \Omega$. To calculate the inner integral along the z-axis, we may divide the elevation $z_0(x)$ into $N_z - 1$ $(N_z \geq 2)$ parts, and eq. (11) becomes

$$\sum_{i=1}^{N_x-1} \left[\int_{x_i}^{x_{i+1}} \int_0^{z_0(x)} F(\sigma, \tilde{G}, \nabla \tilde{G}) \mathrm{d}x \mathrm{d}z = \sum_{i=1}^{N_x-1} \sum_{j=1}^{N_z-1} \int_{x_i}^{x_{i+1}} \left[\int_{z_j(x)}^{z_{j+1}(x)} F(\sigma, \tilde{G}, \nabla \tilde{G}) \mathrm{d}z \right] \mathrm{d}x, \right. \tag{12}$$

where $z_1(x) = 0$, $z_{N_z}(x) = z_0(x)$ and $z_j(x) = (j - 1) z_0(x)/(N_z - 1)$ may be the subsurfaces of the model or mathematical boundaries. Particularly, if $N_x = 2$ and $N_z = 2$, which means $x_i = x_1$, $z_j(x) = 0$ and $x_{i+1} = x_2$, $z_{j+1}(x) = z_0(x)$, the subdomain Ω_{ij} becomes the global

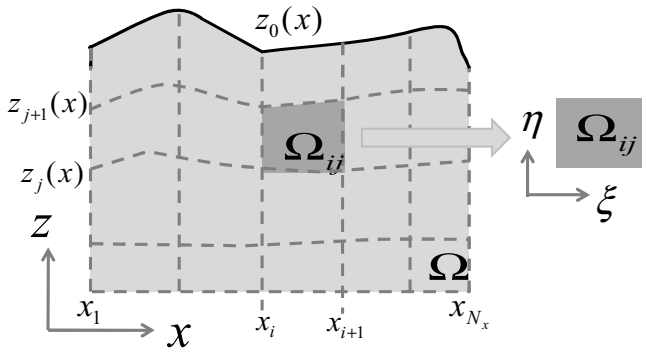

Figure 1. Model having topographic surface $z_0(x)$ and transformation of coordinates from (x, z) to new coordinates (ξ, η) in the model subdomains.

Ω. To this, we apply the variable replacement in the subdomain Ω_{ij} $[x_i, x_{i+1}]\times[z_j(x), z_{j+1}(x)]$, see Fig. 1.

$$x(\xi) = \left(\frac{x_{i+1}-x_i}{2}\right)\xi + \left(\frac{x_i+x_{i+1}}{2}\right), \in [-1, 1],$$
$$z(\xi,\eta) = \left[\frac{z_{j+1}(x)-z_j(x)}{2}\right]\eta + \left[\frac{z_j(x)+z_{j+1}(x)}{2}\right], \eta \in [-1, 1], \tag{13}$$

and obtain the Jacobian matrix

$$\frac{\partial(x,z)}{\partial(\xi,\eta)} = \begin{vmatrix} \frac{\partial x}{\partial \xi} & \frac{\partial z}{\partial \xi} \\ \frac{\partial x}{\partial \eta} & \frac{\partial z}{\partial \eta} \end{vmatrix} = \frac{1}{4}(x_{i+1}-x_i)[(z_{j+1}(x)-z_j(x)]. \tag{14}$$

Applying Gaussian quadrature formulae (Abramowitz & Stegun 1964) to the double intervals in eq. (12) yields

$$\begin{aligned}\int_{x_i}^{x_{i+1}}\left[\int_{z_j(x)}^{z_{j+1}(x)} F(\sigma,\tilde{G},\nabla\tilde{G})\mathrm{d}z\right]\mathrm{d}x &= \int_{-1}^{1}\int_{-1}^{1} F(\sigma,\tilde{G},\nabla\tilde{G})\left|\frac{\partial(x,z)}{\partial(\xi,\eta)}\right|\mathrm{d}\xi\,\mathrm{d}\eta \\ &= \sum_{k=1}^{N_\xi^i}\sum_{l=1}^{N_\eta^j}\frac{1}{4}w_k^i w_l^j (x_{i+1}-x_i)\left\{[z_{j+1}(x)-z_j(x)]F(\sigma,\tilde{G},\nabla\tilde{G})\right\}_{(\xi_k,\eta_l)},\end{aligned} \tag{15}$$

where (ξ_k, η_l) and (w_k^i, w_1^j) are the Gaussian quadrature abscissae and weights respectively in the 2-D case, and they can be analytically calculated, once the integers N_ξ^i and $N^j{}_\eta$ are given for the subdomains (Abramowitz & Stegun 1964). According to the Gaussian quadrature theory, the accuracy of the integration depends on the number of the abscissae N_ξ^i and N_η^j, and it converges exponentially. We simply call the abscissa number per dimension in the subdomain the Gaussian quadrature order. All of the abscissae form a grid, which we call the GQG that spans the whole domain Ω and may easily fit the topography of the Earth's surface, even the subsurface interfaces. From eq. (15), one can see that the key step is to calculate the values of $F(\sigma, \tilde{G}, \nabla\tilde{G})$ at the Gaussian quadrature abscissae (ξ_k, η_l), which involves sampling the model parameters $\sigma(x(\xi_k), z(\xi_k, \eta_l))$ and the field quantity $\tilde{G}(x(\xi_k), z(\xi_k, \eta_l))$,and calculating the gradient $(\nabla\tilde{G})_{(x(\xi_k),z(\xi_k,\eta_l))}$ based on the grid. It is apparent that such grid may give the details of a complex model $\sigma(x, z)$ and the field quantity $\tilde{G}(x, z)$. It differs from the traditional finite element and the spectral element methods, both of which require a powerful mesh generator for fitting a complex topography and the subsurface interfaces in the modelling and assume that each element has constant model parameters (Shewchuk 2002; Rücker *et al.* 2006; Kerry & Weiss 2006).

To calculate the gradient $\nabla\tilde{G} = (\partial\tilde{G}/\partial x, \partial\tilde{G}/\partial z)$, we apply the differential chain rule:

$$\frac{\partial\tilde{G}}{\partial\xi} = \frac{\partial\tilde{G}}{\partial x}\frac{\partial x}{\partial\xi} + \frac{\partial\tilde{G}}{\partial z}\frac{\partial z}{\partial\xi} = \left(\frac{x_{i+1}-x_i}{2}\right)\left[\frac{\partial\tilde{G}}{\partial x} + \left(\frac{\partial z}{\partial\xi}\right)\frac{\partial\tilde{G}}{\partial z}\right], \tag{16}$$

$$\frac{\partial\tilde{G}}{\partial\eta} = \frac{\partial\tilde{G}}{\partial x}\frac{\partial x}{\partial\eta} + \frac{\partial\tilde{G}}{\partial z}\frac{\partial z}{\partial\eta} = \frac{z_{j+1}(x)-z_j(x)}{2}\frac{\partial\tilde{G}}{\partial z}, \tag{17}$$

where $\partial z/\partial\,\xi$ can be calculated by eq. (13). From eqs (16) and (17), we have

$$\begin{aligned}\frac{\partial\tilde{G}}{\partial x} &= \frac{2}{x_{i+1}-x_i}\frac{\partial\tilde{G}}{\partial\xi} - \frac{[z'_{j+1}(x)-z'_j(x)]\eta + [z'_j(x)+z'_{j+1}(x)]}{z_{j+1}(x)-z_j(x)}\frac{\partial\tilde{G}}{\partial\eta}, \\ \frac{\partial\tilde{G}}{\partial z} &= \frac{2}{z_{j+1}(x)-z_j(x)}\frac{\partial\tilde{G}}{\partial\eta}.\end{aligned} \tag{18}$$

We approximate the field quantity $\tilde{G}$ in the domain $(\xi_k, \eta_l) \in[-1,1] \times [-1,1]$ (see eq. 13) by Lagrange interpolation

$$\tilde{G}(\xi,\eta) = \sum_{p=1}^{N_\xi^i}\sum_{q=1}^{N_\eta^j} l_p(\xi)l_q(\eta)\tilde{G}_{pq}. \tag{19}$$

This leads to the derivatives with respect to the Gaussian quadrature abscissae (ξ_k, η_l):

$$\begin{aligned}\left(\frac{\partial\tilde{G}}{\partial\xi}\right)_{kl} &= \sum_{p=1}^{N_\xi^i}\sum_{q=1}^{N_\eta^j} l'_p(\xi_k)l_q(\eta_l)\tilde{G}_{pq} = \sum_{p=1}^{N_\xi^i} l'_p(\xi_k)\tilde{G}_{pl}, \\ \left(\frac{\partial\tilde{G}}{\partial\eta}\right)_{kl} &= \sum_{p=1}^{N_\xi^i}\sum_{q=1}^{N_\eta^j} l_p(\xi_k)l'_q(\eta_l)\tilde{G}_{pq} = \sum_{q=1}^{N_\eta^j} l'_q(\eta_l)\tilde{G}_{kq}.\end{aligned} \tag{20}$$

It should be mentioned that the Lagrangian interpolation (eq. 19) actually has an exponential power convergence for the derivatives (eq. 20) due to employing the Gaussian abscissae as the irregular collocation points, which is the principle of the spectral method (Trefethen

2000). Substituting (20) for (18), we obtain the derivatives with respect to the original coordinates (x, z); they are

$$\left(\frac{\partial \tilde{G}}{\partial x}\right)_{kl} = \sum_{p=1}^{N_\xi^i}\left(\frac{2}{x_{i+1}-x_i}\right)l'_p(\xi_k)\tilde{G}_{pl} + \sum_{q=1}^{N_\eta^j} -\frac{[z'_{j+1}(x)-z'_j(x)]\eta + [z'_j(x)+z'_{j+1}(x)]}{z_{j+1}(x)-z_j(x)}l'_q(\eta_l)\tilde{G}_{kq}$$
$$= \mathbf{N}_x(\xi_k,\eta_l)^T\tilde{\mathbf{G}}^{(x)}, \tag{21}$$
$$\left(\frac{\partial \tilde{G}}{\partial z}\right)_{kl} = \sum_{q=1}^{N_\eta^j}\frac{2l'_q(\eta_l)}{z_{j+1}(x(\xi_k))-z_j(x(\xi_k))}\tilde{G}_{kq} = \mathbf{N}_z(\xi_k,\eta_l)^T\tilde{\mathbf{G}}^{(z)},$$

where

$$\tilde{\mathbf{G}}^{(x)} = \tilde{\mathbf{G}}^{(l)} \cup \tilde{\mathbf{G}}^{(k)},$$
$$\tilde{\mathbf{G}}^{(z)} = \tilde{\mathbf{G}}^{(k)},$$
$$\tilde{\mathbf{G}}^{(l)} = \{\tilde{G}_{pl},\ p = 1, 2, \ldots, N_\xi^i\},$$
$$\tilde{\mathbf{G}}^{(k)} = \{\tilde{G}_{kq}, q = 1, 2, \ldots, N_\eta^j\}, \tag{22}$$

and the components of the vectors $\mathbf{N}_x(\xi_k, \eta_l)$ and $\mathbf{N}_z(\xi_k, \eta_l)$ are calculated as follows

$$N_x(\xi_k,\eta_l)_p = \begin{cases} \left(\frac{2}{x_{i+1}-x_i}\right)l'_p(\xi_k), & (1 \le p \le N_\xi^i); \\ -\frac{[z'_{j+1}(x)-z'_j(x)]\eta+[z'_j(x)+z'_{j+1}(x)]}{z_{j+1}(x)-z_j(x)}l'_p(\eta_l), & N_\xi^i < p \le N_\xi^i + N_\eta^j; \end{cases} \tag{23}$$

$$N_z(\xi_k,\eta_l)_p = \frac{2}{z_{j+1}(x(\xi_k))-z_j(x(\xi_k))}l'_p(\eta_l), \quad (1 \le p \le N_\eta^j). \tag{24}$$

From eq. (21), one can see that the derivative $\partial\tilde{G}/\partial x$ depends on $z'_j(x)$ and $z'_{j+1}(x)$, which are the slopes of the top and bottom boundaries of the subdomain Ω_{ij}(see Fig. 1), which are defined by the topography in the interval $[x_i, x_{i+1}]$. This implies that $z_j(x)$ and $z_{j+1}(x)$ must be differentiable in the interval $[x_i, x_{i+1}]$. The FEM and the spectral element method have no such requirement because they use a constant-element mesh,created by a mesh generator to fit the surface topography or interfaces. However, the requirement can be easily satisfied by appropriate arrangement of the intervals $[x_i, x_{i+1}]$ in terms of the surface topography or interfaces. Therefore, it does not need the mesh generator and can be applied to any topographic surface or interface.

According to eq. (21), we have the following matrix form of the integrand $F(\boldsymbol{\sigma}, \tilde{G}, \nabla\tilde{G})$ for the 2.5-D resistivity case (see eq. 9):

$$\begin{aligned} F(\sigma,\tilde{G},\nabla\tilde{G})\big|_{(\xi_k,\eta_l)} = {} & [\tilde{\mathbf{G}}^{(x)}]^T[\sigma_{xx}(\xi_k,\eta_l)\mathbf{N}_x(\xi_k,\eta_l)\mathbf{N}_x^T(\xi_k,\eta_l)]\tilde{\mathbf{G}}^{(x)} \\ & + [\tilde{\mathbf{G}}^{(z)}]^T[2\sigma_{zx}(\xi_k,\eta_l)\mathbf{N}_z(\xi_k,\eta_l)\mathbf{N}_x^T(\xi_k,\eta_l)]\tilde{\mathbf{G}}^{(x)} \\ & + [\tilde{\mathbf{G}}^{(z)}]^T[\sigma_{zz}(\xi_k,\eta_l)\mathbf{N}_z(\xi_k,\eta_l)\mathbf{N}_z^T(\xi_k,\eta_l)]\tilde{\mathbf{G}}^{(z)} \\ & + k_y^2\sigma_{yy}(\xi_k,\eta_l)\tilde{G}_{kl}. \end{aligned} \tag{25}$$

Therefore, eq. (12) becomes

$$\int_{x_i}^{x_{i+1}}\int_{z_j(x)}^{z_{j+1}(x)} F(\sigma,\tilde{G},\nabla\tilde{G})\mathrm{d}z\mathrm{d}x = \sum_{k=1}^{N_\xi^i}\sum_{l=1}^{N_\eta^j}\left\{\sum_{\substack{p\in(x,z)\\ q\in(x,z)}}\left[\tilde{\mathbf{G}}^{(p)}\right]^T\left[w_{kl}^{(pq)}\mathbf{N}_p(\xi_k,\eta_l)\mathbf{N}_q^T(\xi_k,\eta_l)\right]\tilde{\mathbf{G}}^{(q)} + w_{kl}^{(yy)}k_y^2\tilde{G}_{kl}^2\right\} \tag{26}$$

where

$$w_{kl}^{(pq)} = \frac{1}{4}(x_{i+1}-x_i)[z_{j+1}(x(\xi_k))-z_j(x(\xi_k))]w_k^i w_l^j(\sigma_{pq})_{(\xi_k,\eta_l)}. \tag{27}$$

The boundary integral in eq. (10) may be calculated in terms of the three sides: left-hand (L), right-hand (R) and bottom (B). They are

$$\begin{aligned} \int_L \nu\tilde{G}^2\mathrm{d}\Gamma &= \int_0^{z(x_1)}\nu\tilde{G}^2dz = \sum_{j=1}^{N_z-1}\int_{z_j(x_1)}^{z_{j+1}(x_1)}\nu\tilde{G}^2\mathrm{d}\eta \\ &= \sum_{j=1}^{N_z-1}\sum_{l=1}^{N_\eta^j}\frac{1}{2}[z_{j+1}(x_1)-z_j(x_1)]w_l^j\nu_l\tilde{G}_{jl}^2, \end{aligned} \tag{28}$$

$$\begin{aligned} \int_R \nu\tilde{G}^2\mathrm{d}\Gamma &= \int_0^{z_0(x_{N_x})}\nu\tilde{G}^2\mathrm{d}z = \sum_{j=1}^{N_z-1}\int_{z_j(x_{N_x})}^{z_{j+1}(x_{N_x})}\nu\tilde{G}^2\mathrm{d}\eta \\ &= \sum_{j=1}^{N_z-1}\sum_{l=1}^{N_\eta^j}\frac{1}{2}[z_{j+1}(x_{N_x})-z_j(x_{N_x})]w_l^j\nu_l\tilde{G}_{jl}^2, \end{aligned} \tag{29}$$

$$\int_B \nu\tilde{G}^2 \mathrm{d}\Gamma = \int_{x_1}^{x_{N_x}} \nu\tilde{G}^2 \mathrm{d}x = \sum_{i=1}^{N_x-1} \frac{(x_{i+1}-x_i)}{2} \int_{-1}^{1} \nu\tilde{G}^2 \mathrm{d}\xi$$
$$= \sum_{i=1}^{N_x-1} \sum_{k=1}^{N_\xi^i} \frac{(x_{i+1}-x_i)}{2} w_k^i \nu_k \tilde{G}_{ik}^2. \tag{30}$$

Substituting eqs (26)–(30) for (9), we finally have the matrix form of the functional for 2.5-D resistivity modelling

$$\Psi(\tilde{\mathbf{G}}) = \frac{1}{2}(\tilde{\mathbf{G}}^{\mathbf{T}} M \tilde{\mathbf{G}}) + \mathbf{b}_s \tilde{\mathbf{G}}, \tag{31}$$

where $\tilde{\mathbf{G}}$ is the vector consisting of the values at all points of the Gaussian quadrature grid, $\mathbf{M}$ is the symmetric matrix assembled by the local matrices $w_{kl}^{(pq)} N_p(\xi_k, \eta_l) N_q^T(\xi_k, \eta_l)$ and the coefficients in eqs (26)–(30) and $\mathbf{b}_s$ is the source vector containing the interpolation functions, so that the equation $\tilde{G}_s = \mathbf{b}_s^T \tilde{\mathbf{G}}$ is satisfied. Therefore, the forward modelling reduces to solving the linear equation system

$$M\tilde{\mathbf{G}} = \mathbf{b}_s. \tag{32}$$

DISCRETIZATION OF A 3-D FUNCTIONAL

For 3-D resistivity modelling, the subsurface geological model may be given over the domain $(x, y, z) \in [x_1, x_{N_x}] \times [y_1, y_{N_y}] \times [0, z_0(x, y)]$, where the function $z_0(x, y)$ specifies the 3-D topography of the Earth's surface. We divide the rectangular xy-domain $[x_1, x_{N_x}] \times [y_1, y_{N_y}]$ into sequential rectangles $\square_{ij}$: $[x_i, x_{i+1}] \times [y_j, y_{j+1}]$ $(i = 1, 2, \ldots, N_x - 1; j = 1, 2, \ldots, N_y - 1, N_x \geq 2, N_y \geq 2)$ in which the topography $z_0(x, y)$ is differentiable, $z_0(x, y) \in C^1(\square_{ij})$, and the functional of the 3-D case can be calculated by summing the integrals over the rectangles

$$\int_\Omega F(\boldsymbol{\sigma}, G, \nabla G)\mathrm{d}\Omega = \sum_{i=1}^{N_x-1} \sum_{j=1}^{N_y-1} \int_{x_i}^{x_{i+1}} \int_{y_j}^{y_{j+1}} [\int_0^{z_0(x,y)} F(\boldsymbol{\sigma}, G, \nabla G)\mathrm{d}z]\mathrm{d}x\mathrm{d}y \tag{33}$$

In a similar manner to the 2.5-D case, we break the elevation $z_0(x, z)$ into $N_z - 1$ $(N_z \geq 2)$ parts and eq. (33) becomes

$$\int_\Omega F(\boldsymbol{\sigma}, G, \nabla G)d\Omega = \sum_{i=1}^{N_x-1} \sum_{j=1}^{N_y-1} \sum_{k=1}^{N_z-1} \int_{x_i}^{x_{i+1}} \int_{y_j}^{y_{j+1}} [\int_{z_k(x,y)}^{z_{k+1}(x,y)} F(\boldsymbol{\sigma}, G, \nabla G)\mathrm{d}z]\mathrm{d}x\mathrm{d}y, \tag{34}$$

Here $z_k(x, y) = z_0(x, y)(k - 1)/(N_z - 1)$. Then applying the following variable replacements in the subdomain: $[x_i, x_{j+1}] \times [y_j, y_{j+1}] \times [z_k(x, y), z_{k+1}(x, y)]$

$$x(\xi) = \frac{(x_{i+1}-x_i)}{2}\xi + \frac{(x_i + x_{i+1})}{2},$$
$$y(\eta) = \frac{(y_{j+1}-y_j)}{2}\eta + \frac{(y_j + y_{j+1})}{2}, \tag{35}$$
$$z(\xi, \eta, \varsigma) = \frac{z_{k+1}(x, y) - z_k(x, y)}{2}\varsigma + \frac{z_k(x, y) + z_{k+1}(x, y)}{2},$$

we have the following expression for the triple integrals

$$\int_{x_i}^{x_{i+1}} \int_{y_j}^{y_{j+1}} \int_{z_k(x,y)}^{z_{k+1}(x,y)} F(\sigma, G, \nabla G)\mathrm{d}x\mathrm{d}y\mathrm{d}z = \int_{-1}^{1}\int_{-1}^{1}\int_{-1}^{1} F(\sigma, G, \nabla G) \left|\frac{\partial(x, y, z)}{\partial(\xi, \eta, \varsigma)}\right| \mathrm{d}\xi\mathrm{d}\eta\mathrm{d}\varsigma, \tag{36}$$

where

$$\frac{\partial(x, y, z)}{\partial(\xi, \eta, \varsigma)} = \begin{vmatrix} \frac{\partial x}{\partial \xi} & \frac{\partial y}{\partial \xi} & \frac{\partial z}{\partial \xi} \\ \frac{\partial x}{\partial \eta} & \frac{\partial y}{\partial \eta} & \frac{\partial z}{\partial \eta} \\ \frac{\partial x}{\partial \varsigma} & \frac{\partial y}{\partial \varsigma} & \frac{\partial z}{\partial \varsigma} \end{vmatrix} = \frac{1}{8(N_z - 1)}(x_{i+1} - x_i)(y_{j+1} - y_j)z_0(x, y). \tag{37}$$

Applying the Gaussian quadrature formula (Abramowitz & Stegun 1964) to eq. (36), we obtain the following form:

$$\int_{x_i}^{x_{i+1}} \int_{y_j}^{y_{j+1}} \int_{z_k(x,y)}^{z_{k+a}(x,y)} F(\sigma, G, \nabla G)\mathrm{d}x\mathrm{d}y\mathrm{d}z$$
$$= \sum_{\alpha=1}^{N_\xi^i} \sum_{\beta=1}^{N_\eta^j} \sum_{\gamma=1}^{N_\varsigma^k} \frac{(x_{i+1} - x_i)(y_{j+1} - y_j)z_0(x(\xi_\alpha), y(\eta_\beta))}{8(N_z - 1)} w_\alpha^i w_\beta^j w_\gamma^k \; F(\sigma, G, \nabla G)|_{(\xi_\alpha, \eta_\beta, \varsigma_\gamma)}. \tag{38}$$

Now, we turn to computing the integrand $F(\sigma, G, \nabla G)$ at the Gaussian quadrature abscissae $(\xi_\alpha, \eta_\beta, \varsigma_\gamma)$. Reviewing eq. (35), the field quantity G is a function of the Gaussian quadrature coordinates, for example, $G = G(x(\xi), y(\eta), z(\xi, \eta, \varsigma))$, which gives rise to the following

derivatives using the differential chain rule

$$\begin{aligned}
\frac{\partial G}{\partial \xi} &= \frac{(x_{i+1}-x_i)}{2}\left\{\frac{\partial G}{\partial x}+\frac{(\varsigma+2k-1)}{2(N_z-1)}\frac{\partial z_0(x,y)}{\partial x}\frac{\partial G}{\partial z}\right\},\\
\frac{\partial G}{\partial \eta} &= \frac{(y_{j+1}-y_j)}{2}\left\{\frac{\partial G}{\partial y}+\frac{(\varsigma+2k-1)}{2(N_z-1)}\frac{\partial z_0(x,y)}{\partial y}\frac{\partial G}{\partial z}\right\},\\
\frac{\partial G}{\partial \varsigma} &= \frac{z_0(x(\xi),y(\eta))}{2(N_z-1)}\frac{\partial G}{\partial z}.
\end{aligned} \tag{39}$$

From the above, we obtain the derivatives with respect to the original coordinates (x, y, z):

$$\begin{aligned}
\frac{\partial G}{\partial x} &= \frac{2}{(x_{i+1}-x_i)}\frac{\partial G}{\partial \xi}-\frac{(\varsigma+2k-1)}{z_0(x(\xi),y(\eta))}\frac{\partial z_0(x,y)}{\partial x}\frac{\partial G}{\partial \varsigma},\\
\frac{\partial G}{\partial y} &= \frac{2}{(y_{j+1}-y_j)}\frac{\partial G}{\partial \eta}-\frac{(\varsigma+2k-1)}{z_0(x(\xi),y(\eta))}\frac{\partial z_0(x,y)}{\partial y}\frac{\partial G}{\partial \varsigma},\\
\frac{\partial G}{\partial z} &= \frac{2(N_z-1)}{z_0(x(\xi),y(\eta))}\frac{\partial G}{\partial \varsigma}.
\end{aligned} \tag{40}$$

where G may be expressed by the Lagrange interpolation formula:

$$G(\xi,\eta,\varsigma)=\sum_{p=1}^{N_\xi^i}\sum_{q=1}^{N_\eta^j}\sum_{v=1}^{N_\varsigma^k} l_p(\xi)l_q(\eta)l_v(\varsigma)G_{pqv}. \tag{41}$$

Therefore, we have

$$\begin{aligned}
\left.\frac{\partial G}{\partial \xi}\right|_{(\xi_\alpha,\eta_\beta,\varsigma_\gamma)} &= \sum_{p=1}^{N_\xi^i} l'_p(\xi_\alpha)G_{p\beta\gamma},\\
\left.\frac{\partial G}{\partial \eta}\right|_{(\xi_\alpha,\eta_\beta,\varsigma_\gamma)} &= \sum_{q=1}^{N_\eta^j} l'_q(\eta_\beta)G_{\alpha q\gamma},\\
\left.\frac{\partial G}{\partial \varsigma}\right|_{(\xi_\alpha,\eta_\beta,\varsigma_\gamma)} &= \sum_{v=1}^{N_\varsigma^k} l'_v(\varsigma_\gamma)G_{\alpha\beta v}.
\end{aligned} \tag{42}$$

Substituting (42) for (40), we obtain the gradients

$$\begin{aligned}
\left.\frac{\partial G}{\partial x}\right|_{(\xi_\alpha,\eta_\beta,\varsigma_\gamma)} &= \sum_{p=1}^{N_\xi^i}\frac{2l'_p(\xi_\alpha)}{(x_{i+1}-x_i)}G_{p\beta\gamma}-\sum_{v=1}^{N_\varsigma^k}\frac{(\varsigma_\gamma+2k-1)l'_v(\varsigma_\gamma)}{z_0(x(\xi_\alpha),y(\eta_\beta))}\frac{\partial z_0(x(\xi_\alpha),y(\eta_\beta))}{\partial x}G_{\alpha\beta v}\\
&= \mathbf{N}_x^T(\xi_\alpha,\eta_\beta,\varsigma_\gamma)\mathbf{G}^{(x)},
\end{aligned} \tag{43}$$

$$\begin{aligned}
\left.\frac{\partial G}{\partial y}\right|_{(\xi_\alpha,\eta_\beta,\varsigma_\gamma)} &= \sum_{q=1}^{N_\eta^j}\frac{2l'_q(\eta_\beta)}{(y_{j+1}-y_j)}G_{\alpha q\gamma}-\sum_{v=1}^{N_\varsigma^k}\frac{(\varsigma_\gamma+2k-1)l'_v(\varsigma_\gamma)}{z_0(x(\xi_\alpha),y(\eta_\beta))}\frac{\partial z_0(x(\xi_\alpha),y(\eta_\beta))}{\partial y}G_{\alpha\beta v}\\
&= \mathbf{N}_y^T(\xi_\alpha,\eta_\beta,\varsigma_\gamma)\mathbf{G}^{(y)},
\end{aligned} \tag{44}$$

$$\left.\frac{\partial G}{\partial z}\right|_{(\xi_\alpha,\eta_\beta,\varsigma_\gamma)} = \sum_{v=1}^{N_\varsigma^k}\frac{2(N_z-1)l'_v(\varsigma_\gamma)}{z_0(x(\xi_\alpha),y(\eta_\beta))}G_{\alpha\beta v} = \mathbf{N}_z^T(\xi_\alpha,\eta_\beta,\varsigma_\gamma)\mathbf{G}^{(z)}, \tag{45}$$

where the vectors $\mathbf{N}_x$, $\mathbf{N}_y$ and $\mathbf{N}_z$ consist of the following components:

$$N_x(\xi_\alpha,\eta_\beta,\varsigma_\gamma)_p = \begin{cases} \frac{2l'_p(\xi_\alpha)}{(x_{i+1}-x_i)}, & (1\le p\le N_\xi^i),\\ \frac{(\varsigma_\gamma+2k-1)l'_p(\varsigma_\gamma)}{z_0(x(\xi_\alpha),y(\eta_\beta))}\frac{\partial z_0(x(\xi_\alpha),y(\eta_\beta))}{\partial x}, & (N_\xi^i\le p\le N_\xi^i+N_\varsigma^k), \end{cases} \tag{46}$$

$$N_y(\xi_\alpha,\eta_\beta,\varsigma_\gamma)_q = \begin{cases} \frac{2l'_q(\eta_\beta)}{(y_{j+1}-y_j)}, & (1\le q\le N_\eta^j),\\ \frac{(\varsigma_\gamma+2k-1)l'_q(\varsigma_\gamma)}{z_0(x(\xi_\alpha),y(\eta_\beta))}\frac{\partial z_0(x(\xi_\alpha),y(\eta_\beta))}{\partial y}, & (N_\eta^j\le q\le N_\eta^j+N_\varsigma^k), \end{cases} \tag{47}$$

$$N_z(\xi_\alpha, \eta_\beta, \varsigma_\gamma)_\nu = \frac{2(N_z-1)l'_\nu(\xi_\gamma)}{z_0(x(\xi_i), y(\eta_j))}, \quad (1 \le \nu \le N_\varsigma^k), \tag{48}$$

and the vectors $\mathbf{G}^{(x)}$, $\mathbf{G}^{(y)}$ and $\mathbf{G}^{(z)}$ are given by

$$\begin{aligned}
&\mathbf{G}^{(x)} = \mathbf{G}^{(\alpha)} \cup \mathbf{G}^{(\gamma)},\\
&\mathbf{G}^{(y)} = \mathbf{G}^{(\beta)} \cup \mathbf{G}^{(\gamma)},\\
&\mathbf{G}^{(z)} = \mathbf{G}^{(\gamma)} = \{G_{\alpha\beta\gamma}, \gamma = 1, 2, \ldots, N_\gamma^k, \forall\alpha, \beta\}\\
&\mathbf{G}^{(\alpha)} = \{G_{\alpha\beta\gamma}, \alpha = 1, 2, \ldots, N_\xi^i, \forall\beta, \gamma\},\\
&\mathbf{G}^{(\beta)} = \{G_{\alpha\beta\gamma}, \beta = 1, 2, \ldots, N_\eta^j, \forall\alpha, \gamma\}.
\end{aligned} \tag{49}$$

Once again, it is clear from Eqs (43) and (44) that the derivatives $\partial G/\partial x$ and $\partial G/\partial y$ require knowledge of the slopes of the topography: $\partial z_0(x, y)/\partial x$ and $\partial z_0(x, y)/\partial y$ in the subdomain $[x_i, x_{i+1}]\times[y_j, y_{j+1}]$. In similar fashion to the 2.5-D case, one can appropriately choose the subdomains $[x_i, x_{i+1}]\times[y_j, y_{j+1}]$ in which the slopes are finite. Accordingly, the integrand for 3-D resistivity modelling (see eq. 10) may be written as follows.

$$\begin{aligned}
F(\boldsymbol{\sigma}, G, \nabla G)|_{(\xi_\alpha,\eta_\beta,\varsigma_\gamma)} &= \left[\sigma_{xx}\left(\frac{\partial G}{\partial x}\right)^2 + \sigma_{yy}\left(\frac{\partial G}{\partial y}\right)^2 + \sigma_{zz}\left(\frac{\partial G}{\partial z}\right)^2\right.\\
&\quad \left. + 2\sigma_{xy}\frac{\partial G}{\partial x}\frac{\partial G}{\partial y} + 2\sigma_{xz}\frac{\partial G}{\partial x}\frac{\partial G}{\partial z} + 2\sigma_{zy}\frac{\partial G}{\partial z}\frac{\partial G}{\partial y}\right]_{(\xi_\alpha,\eta_\beta,\varsigma_\gamma)}\\
&= +[\mathbf{G}^{(x)}]^T[\sigma_{xx}\mathbf{N}_x\mathbf{N}_x^T]_{(\xi_\alpha,\eta_\beta,\varsigma_\gamma)}[\mathbf{G}^{(x)}] + [\mathbf{G}^{(y)}]^T[\sigma_{yy}\mathbf{N}_y\mathbf{N}_y^T]_{(\xi_\alpha,\eta_\beta,\varsigma_\gamma)}[\mathbf{G}^{(y)}]\\
&\quad + [\mathbf{G}^{(z)}]^T[\sigma_{zz}\mathbf{N}_z\mathbf{N}_z^T]_{(\xi_\alpha,\eta_\beta,\varsigma_\gamma)}[\mathbf{G}^{(z)}] + [\mathbf{G}^{(x)}]^T[(2\sigma_{xy})\mathbf{N}_x\mathbf{N}_y^T]_{(\xi_\alpha,\eta_\beta,\varsigma_\gamma)}[\mathbf{G}^{(y)}]\\
&\quad + [\mathbf{G}^{(x)}]^T[2\sigma_{xz}\mathbf{N}_x\mathbf{N}_z^T]_{(\xi_\alpha,\eta_\beta,\varsigma_\gamma)}[\mathbf{G}^{(z)}] + [\mathbf{G}^{(y)}]^T[2\sigma_{yz}\mathbf{N}_y\mathbf{N}_z^T]_{(\xi_\alpha,\eta_\beta,\varsigma_\gamma)}[\mathbf{G}^{(z)}].
\end{aligned} \tag{50}$$

Substituting eq. (50) for (38), we obtain

$$\int_{x_i}^{x_{i+1}}\int_{y_j}^{y_{j+1}}\int_{\frac{z_0(x,y)}{(N_z-1)}(k-1)}^{\frac{z_0(x,y)}{(N_z-1)}k} F(\mathbf{m}, G, \nabla G)\mathrm{d}x\mathrm{d}y\mathrm{d}z = \sum_{\alpha=1}^{N_\xi^i}\sum_{\beta=1}^{N_\eta^j}\sum_{\gamma=1}^{N_\varsigma^k}\left\{\sum_{p,q=x,y,z}[\mathbf{G}^{(p)}]^T[w_{\alpha\beta\gamma}^{(pq)}\mathbf{N}_p\mathbf{N}_q^T]\mathbf{G}^{(q)}\right\}, \tag{51}$$

where

$$w_{\alpha\beta\gamma}^{(pq)} = \frac{(x_{i+1}-x_i)(y_{j+1}-y_j)z_0(x(\xi_\alpha), y(\eta_\beta))}{8(N_z-1)}w_\alpha^i w_\beta^j w_\gamma^k(\sigma_{pq})_{(\xi_\alpha,\eta_\beta,\varsigma_\gamma)}. \tag{52}$$

The boundary integral in eq. (10) then consists of the following five parts

$$\int_\Gamma \nu G^2 d\Gamma = \left(\int_{x_1}^{x_{N_x}}\int_0^{z_0(x,y_1)} + \int_{x_1}^{x_{N_x}}\int_0^{z_0(x,y_{N_y})} + \int_{y_1}^{y_{N_y}}\int_0^{z_0(x_1,y)} + \int_{y_1}^{y_{N_y}}\int_0^{z_0(x_{N_x},y)} + \int_{x_1}^{x_{N_x}}\int_{y1}^{y_{N_y}}\right)\nu G^2\mathrm{d}\Gamma, \tag{53}$$

in which the right-hand side integrals are calculated by

$$\int_{x_1}^{x_{N_x}}\int_0^{z_0(x,y_1)}\nu G^2\mathrm{d}x\mathrm{d}z = \sum_{i=1}^{N_x-1}\sum_{k=1}^{N_z-1}\left[\sum_{\substack{1\le\alpha\le N_\xi^i\\1\le\gamma\le N_\varsigma^k}}\frac{(x_{i+1}-x_i)z_0(x(\xi_\alpha), y_1)}{4(N_z-1)}w_\alpha^i w_\gamma^k\nu_{(\xi_\alpha,\varsigma_\gamma)}G_{\alpha 1\gamma}^2\right], \tag{54}$$

$$\int_{x_1}^{xN_x}\int_0^{z_0(x,y_{N_y})}\nu G^2\mathrm{d}x\mathrm{d}z = \sum_{i=1}^{N_x-1}\sum_{k=1}^{N_z-1}\left[\sum_{\substack{1\le\alpha\le N_\xi^i\\1\le\gamma\le N_\varsigma^k}}\frac{(x_{i+1}-x_i)z_0(x(\xi_\alpha), y_{N_y})}{4(N_z-1)}w_\alpha^i w_\gamma^k\nu_{(\xi_\alpha,\varsigma_\gamma)}G_{\alpha N_\eta^{N_y}\gamma}^2\right], \tag{55}$$

$$\int_{y_1}^{y_{N_y}}\int_0^{z_0(x_1,y)}\nu G^2\mathrm{d}x\mathrm{d}z = \sum_{j=1}^{N_y-1}\sum_{k=1}^{N_z-1}\left[\sum_{\substack{1\le\beta\le N_\eta^j\\1\le\gamma\le N_\varsigma^k}}\frac{(y_{j+1}-y_j)z_0(x_1, y(\eta_\beta))}{4(N_z-1)}w_\beta^j w_\gamma^k\nu_{(\eta_\beta,\varsigma_\gamma)}G_{1\beta\gamma}^2\right], \tag{56}$$

$$\int_{y_1}^{y_{N_y}}\int_0^{z_0(x_{N_x},y)}\nu G^2\mathrm{d}x\mathrm{d}z = \sum_{j=1}^{N_y-1}\sum_{k=1}^{N_z-1}\left[\sum_{\substack{1\le\beta\le N_\eta^j\\1\le\gamma\le N_\varsigma^k}}\frac{(y_{j+1}-y_j)z_0(x_{N_x}, y(\eta_\beta))}{4(N_z-1)}w_\beta^j w_\gamma^k\nu_{(\eta_\beta,\varsigma_\gamma)}G_{N_\xi^{N_x}\beta\gamma}^2\right], \tag{57}$$

$$\int_{x_1}^{x_{N_x}}\int_{y_1}^{y_{N_y}} \nu G^2 \mathrm{d}x\,\mathrm{d}z = \sum_{i=1}^{N_x-1}\sum_{j=1}^{N_y-1}\left[\sum_{\substack{1\le\alpha\le N_\xi^i\\ 1\le\gamma\le N_\varsigma^k}} \frac{(x_{i+1}-x_i)(y_{j+1}-y_j)}{4} w_\alpha^i w_\beta^j \nu_{(\xi_\alpha,\eta_\beta)} G^2_{\alpha\beta 1}\right]. \tag{58}$$

Substituting eqs (51) and (54)–(58) for (10), one obtains the same quadratic form as eq. (31), so that the 3-D modelling problem reduces to solving a linear equation system like eq. (32).

TESTING THE PARTIAL DERIVATIVE APPROXIMATIONS

The discretizations of 2-D and 3-D functionals described above contain the gradient of the Green's functions $\nabla\tilde{G} = (\partial\tilde{G}/\partial x, \partial\tilde{G}/\partial z)$ and $\nabla G = (\partial G/\partial x, \partial G/\partial y, \partial G/\partial z)$, which are crucial quantities for the numerical modelling. We may employ either global or local Gaussian quadrature abscissa to calculate the functionals (2-D/3-D integrations) and the gradients. Fig. 2 gives examples of the two abscissa schemes in which we include an undulating surface topography in the model to take account of the skew i.e lack of alignment of grid points in the horizontal direction for a given depth. In the spectral method, the global abscissa in each direction are employed in an orthogonal function series, such as Chebyshev or Fourier series, to achieve high accuracy of the derivatives, but it leads to a fully filled-in matrix (Trefethen 2000) and is very expensive in terms of the cost of computer memory and run time for large 3-D modelling. To obtain a sparse matrix, we apply the global abscissa (Fig. 2a) to the integrations but calculate the gradient with the local cardinal functions obtained by certain neighbouring points rather than the orthogonal function series. We still name it a 'global scheme' to differentiate it from the 'local scheme' (Fig. 2b) that applies Gaussian quadrature abscissae to both the integrations and the gradients in the subdomains that make up the whole model and whose conductivity tensors are variable point by point rather than held constant.

To assess the validity of the approximations made, we use a simple 2-D analytic example for the function $f(x, y) = A\cos(2\pi x/L_x)\sin(2\pi y/L_y)$. Obviously the vertical derivatives $\partial f/\partial z$ should be easier to deal with because all GQG points align in a vertical direction at each horizontal position (see Fig. 2). However, the horizontal derivatives $\partial f/\partial x$ are more challenging because there is no horizontal alignment of grid points at any given depth. For the particular function in question, exact analytic solutions are available for the derivatives, which we can compare with the numerical derivatives. Fig. 3 (upper panel) shows the derivatives using the global scheme ($N_x = 2$, $N_z = 2$, the abscissae equal to 151 and 76 in the x- and z-directions, respectively, and the local cardinal functions of five neighbouring points to compute

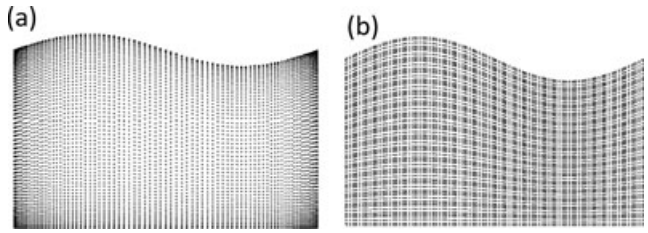

Figure 2. Gaussian quadrature grids for an undulating surface topography: (a) global scheme ($N_x = N_z = 2$, 151 and 76 abscissea in the x- and z-directions, five neighbouring points for the local cardinal function) and (b) local scheme ($N_x = 31$, $N_z = 17$; five abscissae in each direction in a subdomain).

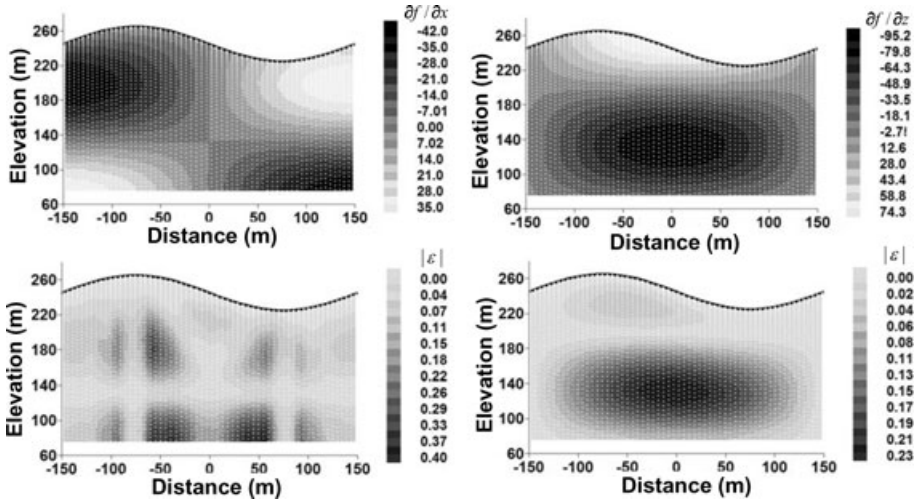

Figure 3. Approximations to the partial derivatives on the Gaussian quadrature grid using the global abscissa shown in Fig. 2a for a simple analytic case $f(x, z) = A\cos(2\pi x/L_x)\sin(2\pi z/L_z)$. The upper two diagrams show the numerical derivatives $\partial f/\partial x$, $\partial f/\partial z$ and the lower diagrams give the absolute errors $|\varepsilon|$. These errors are unacceptably large, and so, a global scheme is not satisfactory.

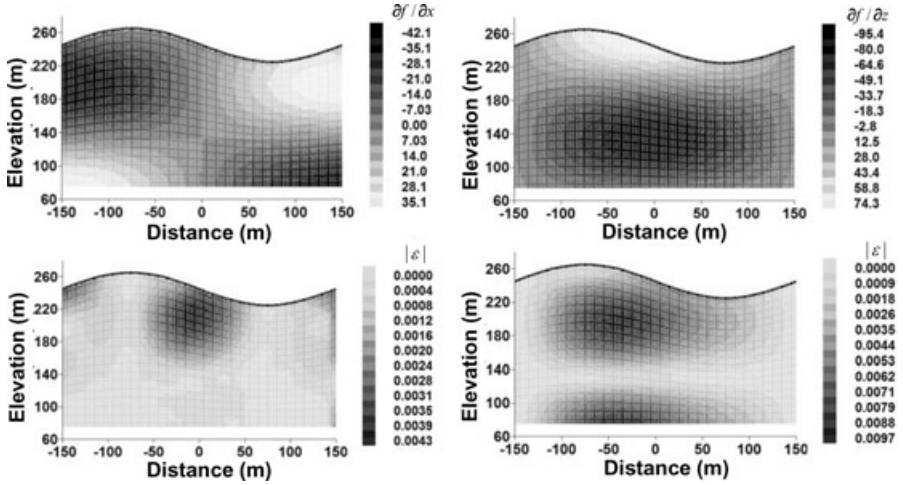

Figure 4. Approximations to the partial derivatives on the Gaussian quadrature grid using the local scheme shown in Fig. 2b for the same analytic example given in Fig 3. The errors (lower diagrams) in the numerical derivatives are now generally less than 0.5per cent.

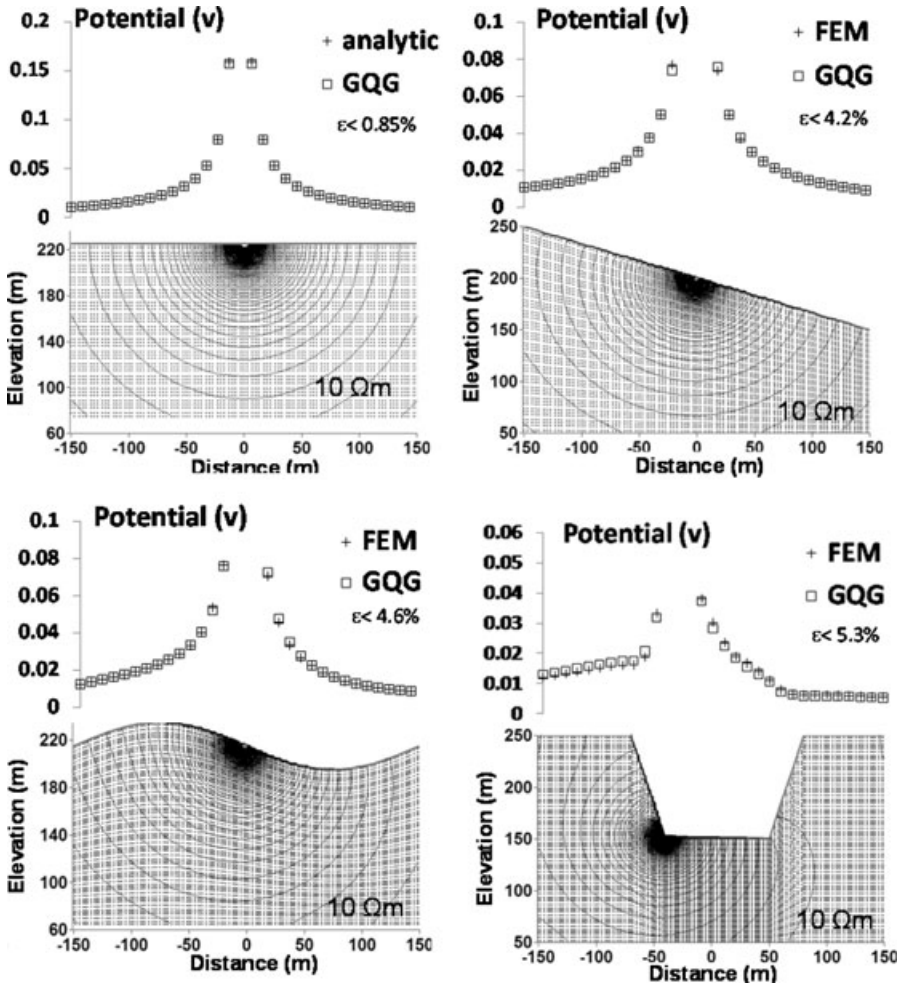

Figure 5. Results of GQG modelling of the electric response for four homogeneous, isotropic models ($\rho = 10$ Ω-m) but incorporating surface topography. Equipotential diagrams are shown in cross-section form along with surface voltage profiles. The surface profiles are compared against the analytic solution (flat topography case) and the finite element solutions (FEM) with the fine rectangular mesh. The slight deviations in vicinity of the source between the FEM solutions and the GQGs are due to the errors in matching of the topography in the FEM.

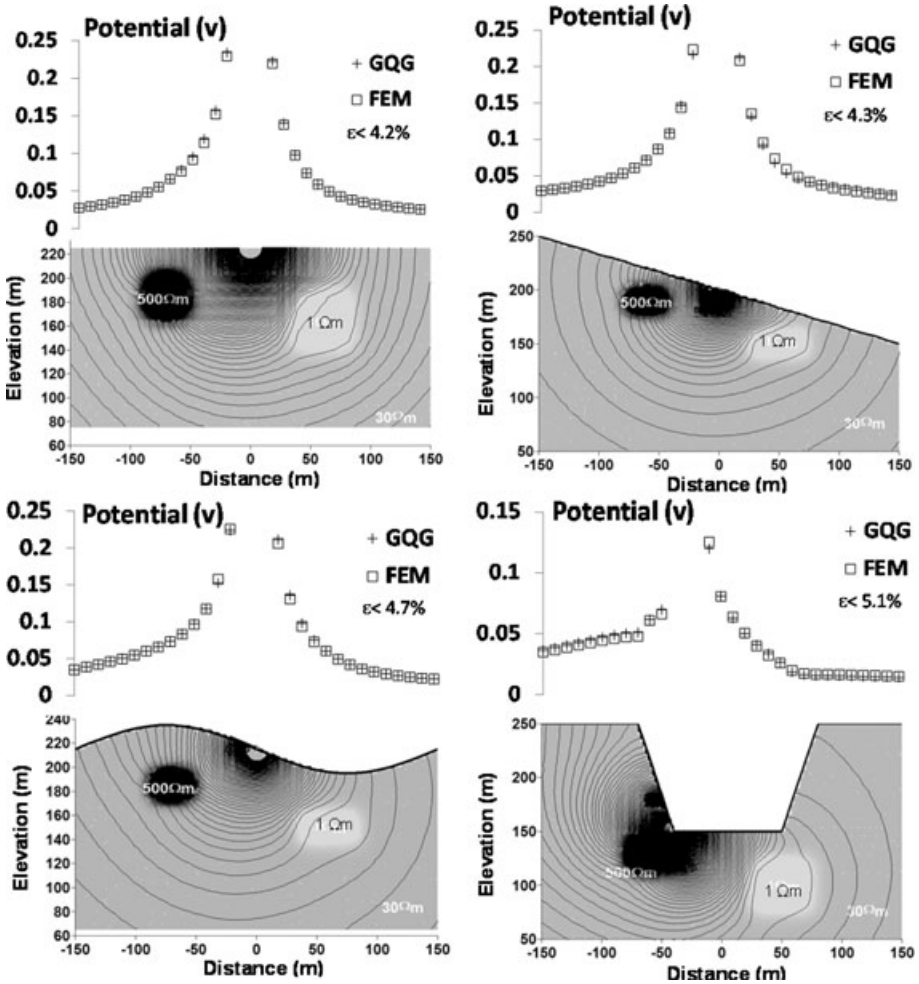

Figure 6. GQG modelling results for four heterogeneous, isotropic models, having the same topography as in previous models (Fig. 5) but now incorporating embedded low and high resistivity blocks(1 and 500 Ω-m) in a background resistivity of 30 Ω-m. Note the distortion of the equipotentials around the anomalous bodies. The surface voltage profiles are compared against the finite element modelling results and found to be comparable.

the derivatives). The bottom panel shows the absolute errors $|\varepsilon|$, which indicates, at some points, the relative error may be as large as 40 per cent. They are worse for the x derivatives because of the staggering or misalignment associated with the surface topography and resultant coordinate stretching. Fig. 4 shows the results, using the local scheme ($N_x = 30$, $N_z = 15$ and 5 abscissae per 10 m). Again, both the actual computed derivatives and the absolute errors relative to the true solution are shown. The errors in this case are much reduced, and generally less than 1 per cent. We have conducted tests for other topographies including a flat surface, a sloping interface and a trench using the same analytic expression. We find that the local scheme does quite a good job (errors less than 1 per cent) in all cases. From the theory of the spectral method (Trefethen 2000), it is not difficult to understand why the 'global scheme' is worse than the local scheme. The neighbouring points for computing the derivatives in the global scheme are actually not the irregular collocation points of the spectral method, but the Gaussian abscissae in the subdomain does fulfil this requirement.

COMPUTATIONAL ASPECTS

We showed above that the GQG method gives rise to a system of linear equations:

$$\begin{aligned} &3-D: \quad \boldsymbol{M}(\boldsymbol{\sigma})\mathbf{G} = \mathbf{b}_s \\ &2.5-D: \quad \boldsymbol{M}(\boldsymbol{\sigma}, k_y)\tilde{\mathbf{G}} = \mathbf{b}_s \end{aligned} \tag{59}$$

where $\boldsymbol{M}(\boldsymbol{\sigma})$ or $M(\sigma, k_y)$ is an $N \times N$ banded symmetric matrix, depending on the conductivity tensor $\boldsymbol{\sigma}$ and the wavenumber k_y, $\mathbf{G}$ or $\tilde{\mathbf{G}}$ is the N-component vector which gives the values of the Green's functions or the wavenumber version (Fourier transformed) of the Green's functions at all grid nodes and $\mathbf{b}_s$ is the source vector which has zero components except for the current magnitude 1 at the current injection location(s). The potential U is simply related to the Green's function G through the relation $U = IG$, where I is the actual current magnitude. Here N is the dimension of the discrete model (total number of the Gaussian quadrature abscissae), and it may be as large as several hundred when tackling a 3-D problem. Solving the linear equation system, one can obtain the potential values corresponding to a current injection

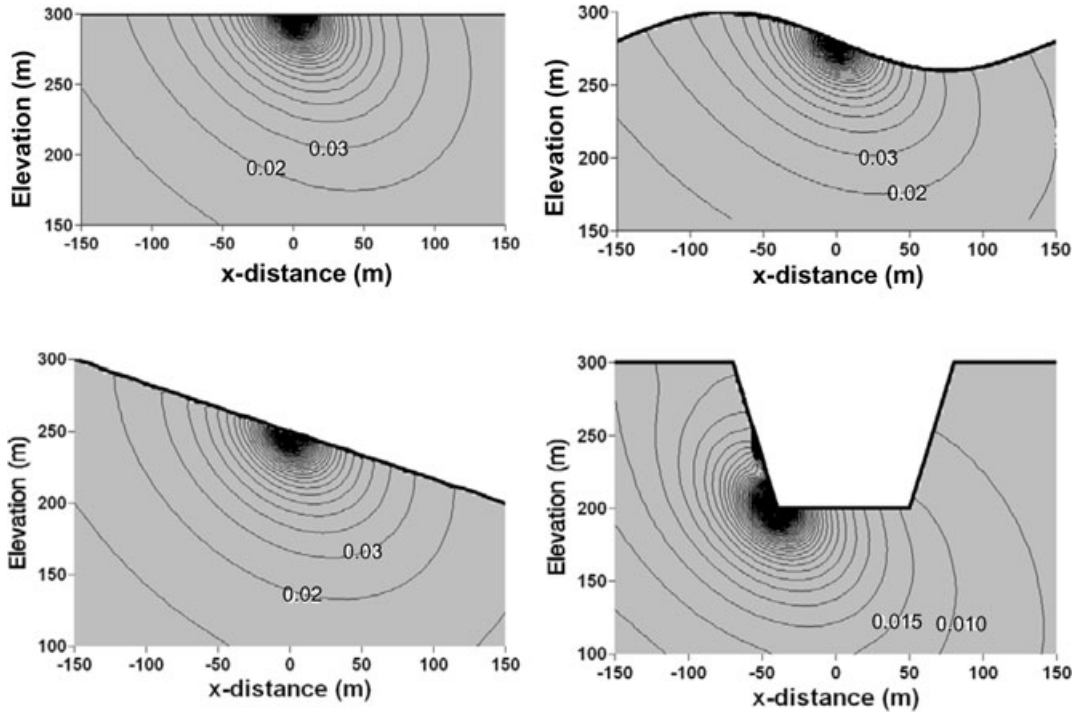

Figure 7. GQG modelling results for four homogeneous, anisotropic models having the same topography as in the isotropic models (Figs 5 and 6). The medium is transversely isotropic, with longitudinal resistivity 5 Ω- m and transverse resistivity 10 Ω-m. The tilt angle of the axis of symmetry is 45°, down to the left-hand side (transverse resistivity direction). The section is aligned perpendicular to strike of the plane of stratification. Note the elliptical shape to the equipotential contours, elongated in the dip direction of the plane of stratification (longitudinal resistivity direction).

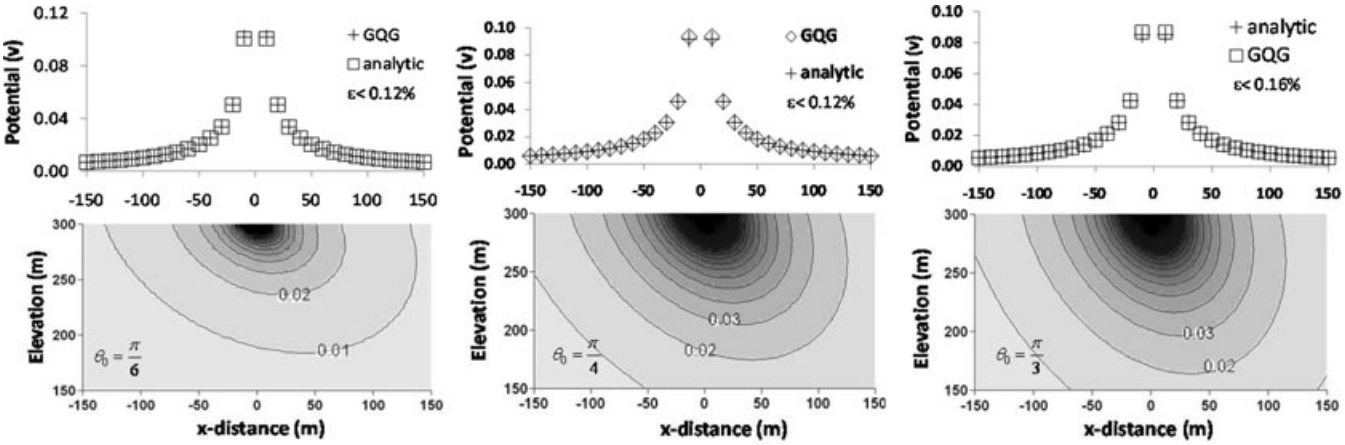

Figure 8. Surface voltage profiles and the potential contour cross-sections for the homogeneous, anisotropic flat topography model of Fig. 7, compared against analytic solutions for transverse isotropic case. Results are given for three angles of dip of the symmetry axis: 30°, 45° and 60°. Note how contours are elongated in the direction of the plane of stratification (longitudinal resistivity direction) and the agreement between numerical and analytic results is excellent.

point. Normally, electric resistivity imaging surveys involve a large number of current electrode positions so that eq. (59) may have to be solved hundreds of times.

In 3-D applications, an efficient and accurate linear equation solver is required. Zhou & Greenhalgh (2001) compared four iterative solvers, based on the pre-conditioned conjugate gradient method, and one on the matrix method (banded Cholesky decomposition, Press *et al*. 1996) in terms of accuracy and efficiency and concluded that the two iterative solvers (symmetric successive over-relaxation algorithm, see Axelsson 1984; Spitzer 1995) and the incomplete Cholesky decomposition algorithm (see David 1978; Ajiz & Jennings 1984; Manolis & Michael 1991; Zhang *et al*. 1995) are suitable options for 3-D modelling. We have shown that in 3-D FEM, if tetrahedral elements are employed then the number of non-zero elements in each row of the matrix $\boldsymbol{M}$ is equal to eight (Zhou & Greenhalgh 2001). By contrast, it is clear from the previous formulation that the GQG method (similar to the spectral element method) has, in general, more than eight non-zero elements, because the minimum number of Gaussian quadrature abscissa is 2 (see eq. 38), This means that if the dimension (N) is the same in each case, the GQG method will consume more computer memory and time, whatever solver is applied.

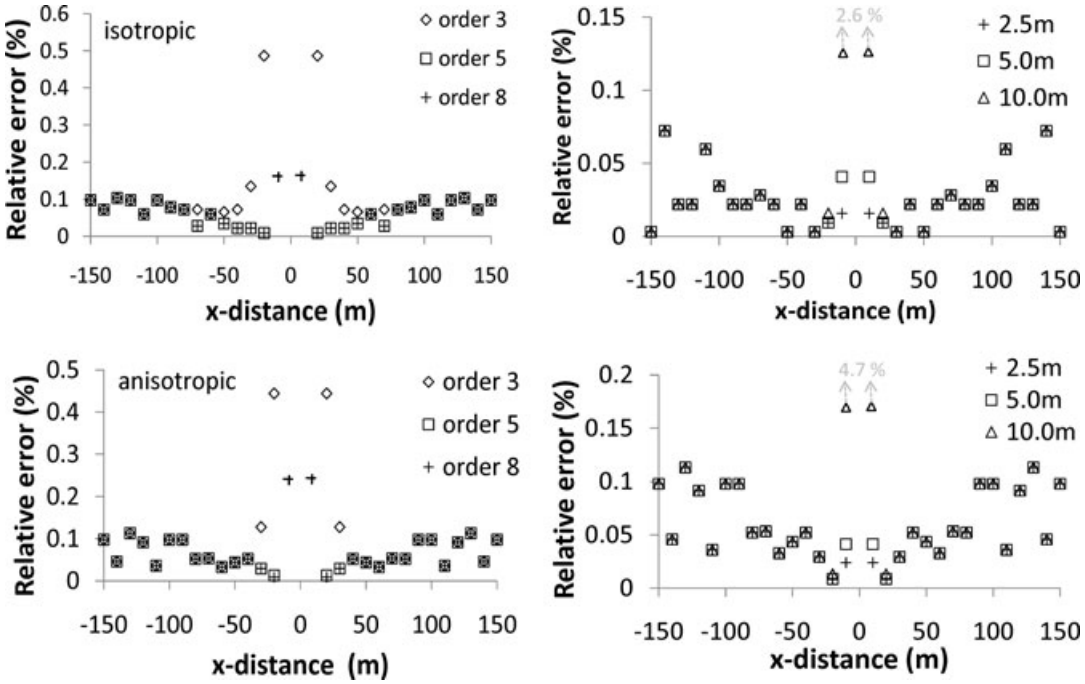

Figure 9. Relative error curves for the homogeneous isotropic (1st row) and anisotropic models (2nd row) having 45° dip of the symmetry axis. In each case three sets of results are given, for different Gaussian quadrature orders (number of the abscissae) and different subdomain sizes. Accuracy near the source increases as the number of abscissae increases and the subdomain size decreases.

In 2.5-D applications, the banded Cholesky decomposition method ($\boldsymbol{M} = \mathbf{L}\mathbf{L}^T$, Press *at al.* 1996) is commonly applied to the linear equation system. The advantage of the matrix method is that the decomposition is carried out only once for all the current electrodes. The cost of computer memory and time depend on the dimension (N) of the matrix $\boldsymbol{M}$ and its bandwidth ($N_{\rm bw}$). The smaller the bandwidth, the faster is the solution procedure. It is not difficult to show that the maximum bandwidth of the FEM (triangular or rectangular elements) and the GQG method (similar to the spectral element method) can be estimated by $N_{\rm bw}^{\rm FEM} = \max\,[N_z(x)] + 1$ (Zhou & Greenhalgh 2000) and $N_{\rm bw}^{\rm GQG} = (N_\xi - 1)\{\max\,[N_z(x)] + 1\}$(see eq. 21), respectively, where $N_z(x)$ is the total number of nodes in the vertical direction at x and N_ξ is the number of Gaussian quadrature abscissae in the x-direction of a subdomain. Obviously, 2.5-D GQG modelling also costs more computer memory and time than 2.5-D FEM because $N_\xi \geq 2$. In addition, for reasons of efficiency and accuracy, only limited wavenumbers are often employed in the modelling. The choice of the limited wavenumbers includes determining the total number and the distribution in the range $k_y \in (0, \infty)$, as well as an appropriate interpolation of $\tilde{G}(k_y)$ for the inverse Fourier cosine transform. Theoretically, the more wavenumbers used, the more accurate is the solution obtained. Several schemes for choosing k_y and the interpolation for $\tilde{G}(k_y)$ have been developed (Dey & Morrison 1979a; Queralt *et al*. 1991; LaBrecque *et al.* 1996; Xu *et al*. 2000). Actually, these schemes are all based on analytic solutions for the simple models, due to the non-existence of any universal scheme to choose the wavenumbers for a general inhomogeneous model. Consequently, the computation errors for 2.5-D modelling are mainly contributed by the use of a limited set of wavenumbers, the discretization of the model and the validity of the artificial mixed boundary condition.

After obtaining the Green's function G, one can easily compute the apparent resistivity $\rho_{\rm a}$ for different electrode configurations by the following formula:

$$\rho_{\rm a} = K\,\Delta G_{MN}, \tag{60}$$

where K is the geometry factor for the specific electrode configuration, which only depends on the positions of the electrodes, and ΔG_{MN} is the potential difference between the two measuring electrodes. This normalized quantity is employed to indicate variation of the resistivity of the subsurface, that is, departures from uniformity.

NUMERICAL EXAMPLES

2.5-D isotropic models with variable topography

First we consider four homogeneous, isotropic models having a fixed resistivity of 10 Ω-m but variable surface topographies. Fig. 5 shows the models and the results obtained. The actual model parts of the GQGs are plotted as the background to the diagrams. The entire GQGs include the extended margins on both sides and the deeper part to reduce the artificial boundary effects. We did not plot the margin parts in any of the diagrams. The plots show equipotential contours in vertical sections for each model, as well as computed profiles of voltage versus distance along the ground surface. The diagram in the upper left-hand panel is for a flat topography, which has an analytical solution.

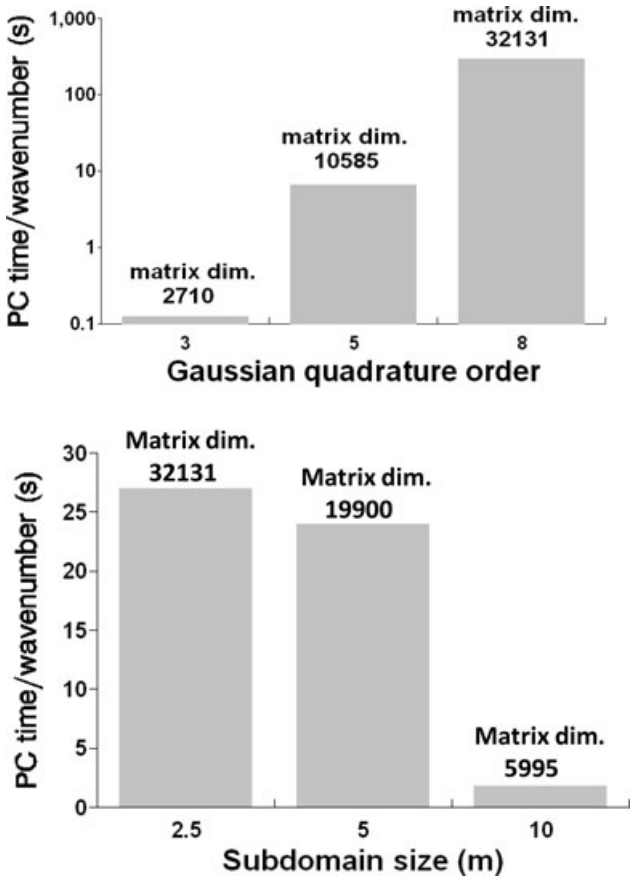

Figure 10. PC time costs of the linear equation solver (LL^T) per wavenumber (Pentium (R) M, 2GHz, 2GB RAM) for three Gaussian quadrature order and three subdomain sizes applied to homogenous anisotropic modelling. Here the dimension of the system matrix is given for each case.

It is plotted against the GQG solution in Fig. 5. The error in the numerical solution is less than 0.85 per cent. This maximum occurs in the vicinity of the current source position. Next we show the results for a sloping surface topography (upper right-hand panel). The GQG solution along the surface is compared with that obtained using a finite element algorithm (Zhou & Greenhalgh 2000), where the sloping surface is approximated by a series of small vertical steps. Agreement between the two results is very good. The equipotential contours are quasi-circular but affected by the topography. The bottom two diagrams are for an undulating surface topography and a prominent trench (or valley). The slight deviations in the vicinity of the source between the FEM solutions and the GQG solutions are due to the errors in exactly matching the topography in our FEM code. In each case, one can see that the contours are roughly circular and all contours meet the surface topography at 90°, implying tangential current flow here (The Neumann boundary condition $J_n = 0$).

Next we show the GQG results for four inhomogeneous isotropic models (Fig. 6). We use the same topographic surfaces as before (flat, inclined, undulated, valley), but now there are low and high resistivity anomalous bodies of 1 and 500 Ω-m, respectively, embedded within the background medium. The rectangular bodies are of approximate dimension 40 m. There is a clear distortion in the equipotential contours compared with the homogeneous case, with the equipotential lines being deflected away from the conductive body (current lines drawn in) and attracted towards the resistor (current lines deflected away). Fig. 6 also shows the surface voltage profiles obtained with each model. We show for comparison the results obtained using a FEM program that uses small steps matching the surface topography. There is good agreement in each case.

2.5-D anisotropic models

Having established the validity of the GQG solutions for isotropic models, we next wish to examine solutions for anisotropic models but also incorporating the same surface topography. The medium is assumed to be transversely isotropic with a tilted axis of symmetry. The transverse resistivity $\rho_t (= 1/\sigma_{z'z'})$ is 10 Ω-m and the longitudinal resistivity $\rho_l (= 1/\sigma_{x'x'} = 1/\sigma_{y'y'})$ is 5 Ω-m, giving a coefficient of anisotropy of 1.4. The angle of tilt of the symmetry axis is 45° down to the left-hand side. This is the transverse resistivity direction. The plane of stratification causing the anisotropy (e.g. bedding plane, fracture plane) dips at 45° down to the right-hand side. This is the longitudinal resistivity direction. We ignore the azimuth angle here and assume that the profile is oriented perpendicular to strike (2.5-D case). Results of the GQG simulations are shown for three topographic models in Fig. 7. Note how the equipotential contours are now elliptical and centred on the source, with the long axis in the longitudinal (lower resistivity) direction. In all models, the Neumann boundary condition is honoured at the ground

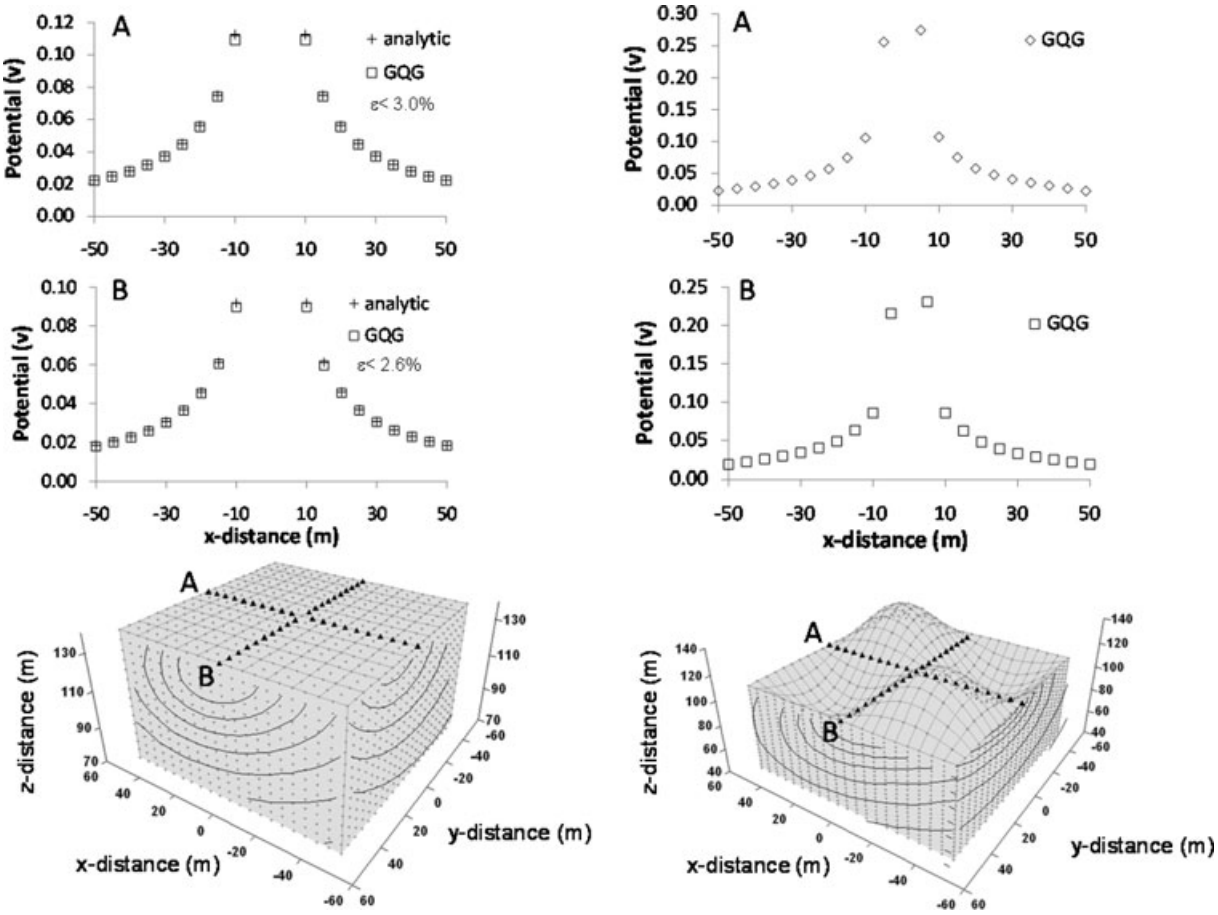

Figure 11. 3-D homogeneous, anisotropic model involving flat surface (left-hand panels), and surface topography (right-hand panel) and the computed subsurface equipotentials. The current source is located on the surface at the centre of each model where the two orthogonal profiles A and B intersect. The computed voltages along each profile are shown above the models. For the flat surface model the analytic solution is also displayed for comparison. The agreement between the GQG results and the analytic solution is excellent.

surface, with current density entirely tangential. The equipotential contours do not perfectly intersect the surface orthogonally because in an anisotropic medium, the current density vector is not parallel to the electric field (which is in a direction perpendicular to the equipotentials).

Analytic solutions exist for the potential at the surface of a uniform, tilted, transversely isotropic half-space having a flat upper surface (Bhattacharya & Patra 1968; eq. 2.35). This corresponds to the model shown in the upper left-hand panel of Fig. 7. In Fig. 8, we show the surface profiles and potential contour sections obtained for this model for three different dips of the symmetry axis: 30°, 45° and 60° (measured from the horizontal). Superimposed on the profiles are the analytic solutions. The agreement between numerical and theoretical results is excellent. In the GQG solution, we used a maximum subdomain size (Ω_{ij}) of 10 m^2 and an order 8 Gaussian quadrature grid. The potential contour sections clearly show the elliptic patterns with the long axis pointing in the direction of the bedding plane (or longitudinal direction). Note how the elliptical patterns steepen as the dip of the plane of stratification (measured from the horizontal) increases.

We have experimented with different subdomain sizes and different orders of the GQG. Fig. 9 shows the errors (compared to the analytic solutions) for three Gaussian quadrature orders: 3, 5 and 8 (left-hand panel), with a fixed subdomain (10 m) and three subdomain sizes: 2.5, 5.0 and 10.0 m (right-hand panel), with orders 3 (2.5 m) and 4 (5.0 and 10.0 m). The graph gives results for isotropic (1st row) and anisotropic models having 45° dip of the symmetry axis (2nd row). Clearly, except near the source, the errors are within acceptable limits (< 1 per cent) in all cases, and even near the source, the errors significantly decreases as more Gaussian quadrature abscissae or smaller subdomain sizes are employed. However, as the number of Gaussian quadrature abscissae increases or the subdomain size deceases, the computing time significantly increases, because the dimension of the matrix in the linear equation system (eq. 32) and the non-zero elements in each row of the matrix increase accordingly. Fig. 10 shows the PC time [Pentium (R) M, 2GHz, 2GB RAM] costs for one wavenumber in these cases. Note the dramatic increase in the diagram from matrix dimension 2710 (order 3) to dimension 32 131 (order 8) and over three orders of magnitude increase in the computation time. Also note that the size of 2.5 m with order 3 has the same matrix dimension (32 131) as the size of 10 m with order 8 and both give satisfactory results (see Fig. 9), but the former costs about 1/5 the computing time of the latter due to reducing the bandwidth of the matrix with the low order. Therefore, there is a balance between the subdomain size and the GQG order for the accuracy and efficiency. One must reach a compromise between them in any modelling.

3-D anisotropic model with topography

Fig. 11 shows two examples of 3-D homogenous anisotropic modelling ($\rho_{x'x'} = \rho_{y'y'} = 5$ Ω-m, $\rho_{z'z'} = 10$ Ω-m, $\theta_0 = 45^\circ$, $\varphi_0 = 0^\circ$). One has a flat surface so that it has an analytic solution for comparison. The other incorporates a complex topography that features two hills and adjacent low lying areas. We have plotted in Fig. 10 the electric potential contour sections in the subsurface obtained from GQG modelling and the voltage profiles obtained for the two orthogonal surface lines shown in the model and labelled A and B. For the flat surface model, the potential curves on the surface are symmetric about the source point in terms of the analytic solution (eq. A1). From the left-hand panel of Fig. 11, we observe excellent agreement between the GQG modelling and the analytic solutions. From the 3-D topographic result (right-hand panel in Fig. 11), one can see the potential curves are no longer symmetric. This change implies the topography effect, which demonstrates the versatility and accuracy of the GQG method.

CONCLUSIONS

We have presented a new Gaussian quadrature grid (GQG) scheme for 2.5-D/3-D DC resistivity modelling. The method is particularly suitable for numerical simulation of a complex geological model, having the most general anisotropy and an arbitrary topographic surface. The formulation shows that it is close to the spectral element method, but it does not require the constant-element mesh matching the topographic Earth surface due to invoking a GQG for the subdomains covering the whole model. Local cardinal functions are used to determine the partial derivatives of the Green's functions at each Gaussian abscissa that appear in the functional to be minimized. Subdomain integration and summation leads to a system of linear equations to be solved, using standard iterative or matrix inversion techniques. The new method is compared against analytic solutions and finite element solutions for both simple and complex models. It was found to be highly accurate, except in the vicinity of the source, and much easier to deal with anisotropic models, having a surface topography than any other traditional numerical method.

ACKNOWLEDGMENT

This research was supported by a grant from the Australian Research Council. The authors thank the Editor and two anonymous reviewers for their comments.

REFERENCES

Abramowitz, M. & Stegun, I., 1964. *Handbook of Mathematical Functions with Formulas, Graphys and Mathematical Tables*, Dover Publications, Inc. New York.

Ajiz, M.A. & Jennings, A., 1984. A robust incomplete Choleski conjugate gradient algorithm, *Int. J. Numer. Meth. Eng.,* **20,** 949–966.

Asten, M.W., 1974. The influence of electrical anisotropy on mise a la masse surveys, *Geophy. Prosp.,* **22,** 238–245.

Axelsson, O., 1984. A survey of pre-conditioned iterative methods for linear systems of equations, *BIT,* **25,** 166–187.

Bhattachary, P.K. & Patra, H.P., 1968. *Direct Current Geoelectric Sounding, methods in Geochemistry and Geophysics,* Elsvier, Amsterdam.

Blome, M. & Maurer, H., 2007. Advances in 3D geoelectric forward solver, in *Proceedings of the 4th International Symposium on Three Dimensional Electromagnetics,* Freiberg, Germany, September 27–30, pp. 7–10.

Boyd, J.P., 1989. *Chebyshev and Fourier Spectral Methods,* Springer-Verlag, Berlin.

Coggon, J.H., 1971. Electromagnetic and electrical modelling by the finite element method, *Geophysics,* **36,** 132–155.

Das, U.C. & Parasnis, D.S., 1987. Resistivity and induced polarisation responses of arbitrary shaped 3-D bodies in a two-layered earth, *Geophys. Prosp.,* **35,** 98–109.

David, S.K., 1978. The incomplete Choleski conjugate gradient method for the iterative solution of systems of linear equations, *J. Comput. Phys.,* **26,** 43–65.

Dey, A. & Morrison, H.F., 1979a. Resistivity modelling for arbitary shaped two-dimensional structures, *Geophys. Prosp.,* **27,** 106–136.

Dey, A. & Morrison, H.F., 1979b. Resistivity modelling for arbitrary shaped three-dimensional structures, *Geophysics,* **44,** 753–780.

Eskola, L., 1992. *Geophysical Interpreation Using Integral Equations,* Chapman and Hall, London, 191 pp.

Fox, R.C., Hohmann, G.W., Killpact, T.J. & Rijo, L., 1980. Topographic effects in resistivity and induced polarization surveys, *Geophysics,* **45,** 75–93.

Graham F.C. & Oden J., 1983. *Finite Elements: A Second Course,* Vol. II, Prentice-Hall Inc., Englewood Cliffs.

Habberjam, G.M., 1972. The effects of anisotropy on square array resistivity measurements, *Geophys. Prosp.,* **20,** 251–266.

Holcombe, H.T. & Jirack, G., 1984. 3-D terrain corrections in resistivity surveys, *Geophysics,* **49,** 439–452.

Hvodara, M. & Kaikkonene, P., 1998. An integral equation solution of the forward DC geoelectric problem for a 3D body of inhomogeneous conductivity buried in a half space, *J. Appl. Geophys.,* **39,** 95–107.

James, B.A., 1985. Efficient microcomputer-based finite difference resistivity modelling via Polozhi decomposition, *Geophysics,* **50,** 443–465.

Kerry, K. & Weiss, C., 2006. Adaptive finite element modelling using unstructured grids, The 2D magnetotelluric example, *Geophysics,* **71,** G291–G294.

Komatitsch, D. & Tromp, J., 1999. Introduction to the spectral element method for the three-dimensional seismic wave propagation, *Geophys. J. Int.,* **139,** 806–822.

LaBrecque, D.J., Miletto, M., Daily, W., Ramirez, A. & Owen, E., 1996. The effects of noise on Occam's inversion of resistività tomography data, *Geophysics,* **61,** 538–548.

Lee, T., 1975. An integral equation and its solution for some two and three dimensional problems in resistivity and induced polarisation, *Geophys. J. Int.,* **42,** 81–95.

Li, Y. & Spitzer, K., 2005. Finite element resistivity modelling for three-dimensional structures with arbitrary anisotropy, *Phys. Earth planet. Inter.,* **150,** 15–27.

Loke, M.H., 2000. Topographic modelling in resistivity imaging inversion, in *Proceedings of the 62nd EAGE Conference & Technical Exhibition* (Extended Abstract, D-2).

Lowry, T., Allen, M.B. & Shive, P.N., 1989. Singularity removal: a refinement of resistivity modelling techniques, *Geophysics,* **54,** 766–774.

Martinec, Z., 1999. Spectral-finite element approach to three-dimensional electromagnetic induction in a spherical earth, *Geophys. J. Int.,* **148,** 229–250.

Manoilis, P. & Michael, C.D., 1991. Improving the efficiency of incomplete Choleski preconditioning, *Comm. Appl. Numer. Meth.,* **7,** 603–612.
Mufti, I.R., 1976. Finite difference resistivity modelling for arbitrary shaped two-dimensional structures, *Geophysics,* **41,** 62–78.
Mundry, E., 1984. Geoelectrical model calculations for two-dimensional resistivity distributions, *Geophys. Prosp.,* **32,** 124–131.
Pain, C., Herwanger, J., Saunders, J., Worthington, M. & Oliveira, C., 2003. Anisotropic resistivity inversion, *Inverse Problems,* **19,** 1081–1111.
Pervago, E., Mousatov, A. & Shevnin, V., 2006. Analytical solution for the electric potential in arbitrary anisotropic layered media applying the set of Hankel transforms of integer order, *Geophys. Prosp.,* **54,** 651–661.
Press, W., Teukolsky, S., Vetterling, W. & Flannery, B., 1996. *Numerical Recipes in Fortran 90, the Art of Parallel Scientific Computing,* Cambridge University Press.
Pridmore, D., Hohmann, G.W., Ward, S.H. & Sill, W.R., 1981. An investigation of the finite element method for electrical and electromagnetic modelling data in three dimensions, *Geophysics,* **46,** 1009–1024.
Queralt, P., Pous, P. & Marcuello, A., 1991. 2D resistivity modelling: an approach to arrays parallel to the strike direction, *Geophysics,* **56,** 941–950.
Rücker, C., Gunther, T. & Spitzer, K., 2006. Three-dimensional modelling and inversion of DC resistivity data incorporating topography, I: Modelling, *Geophys. J. Int.,* **166,** 495–505.
Shewchuk, J.R., 2002. Delaunay refinement algorithms for triangular mesh generation, *Comput. Geometry—Theory & Applications,* **22,** 21–74.
Spitzer, K., 1995. A 3-D finite difference algorithm for DC resistivity modelling using conjugate gradient methods, *Geophys. J. Int.,* **123,** 903–914.
Trefethen, L.N., 2000. *Spectral methods in MATLAB,* SIAM, Philadelphia, PA.
Xu, S.Z., Duan, B.C. & Zhang, D.H., 2000. Selection of wavenumbers k using an optimisation method for the inverse Fourier transform in 2.5D electric modelling, *Geophys. Prosp.,* **48,** 789–796.
Yin, C.H. & Weidelt, P., 1999. Geoelectrical fields in a layered earth with arbitrary anisotropy, *Geophysics,* **64,** 426–434.
Zhang, J., Mackie, R. & Madden, T., 1995. 3-D resistivity forward modelling and inversion using conjugate gradients, *Geophysics,* **60,** 1313–1328.
Zhao, S. & Yedlin, M., 1996. Some refinements on the finite difference method for 3-D DC resistivity modelling, *Geophysics,* **61,** 1301–1307.
Zhou, B. & Greenhalgh, S.A., 2000. Cross-hole resistivity tomography using different electrode configuration, *Geophys. Prosp.,* **48,** 887–912.
Zhou, B. & Greenhalgh, S.A., 2001. Finite element three-dimensional direct current resistivity modelling: accuracy and efficiency considerations, *Geophys. J. Int.,* **145,** 676–688.

APPENDIX A: BOUNDARY CONDITIONS

We have used a mixed Dirichelet/Neumann boundary condition in eqs (6) and (7). Here we derive the expressions for the parameter ν which appears in those equations. Consider a homogeneous anisotropic medium, at least at the position of the boundaries far away from the source. The Green's function of a point source ($I = 1$) located at (0, 0, 0) may simply be written in the form

$$G = \frac{C}{\sqrt{\mathbf{r}^T \cdot \boldsymbol{\rho} \cdot \mathbf{r}}}, \tag{A1}$$

where $\mathbf{r} = (x, y, z)$, C is a constant $= (\det \boldsymbol{\rho}_{ij})^{1/2}/2\pi = (\rho_{x'x'} \,.\rho_{y'y'} \,.\, \rho_{z'z'})^{1/2}/2\pi)$ and ρ ($= [\sigma_{ij}\,]^{-1}$) is the resistivity tensor, the inverse matrix of the conductivity tensor. For a 2.5-D problem ($\rho_{xy} = \rho_{yz} = 0$, see eq. 8a), it becomes

$$G = \frac{C/\sqrt{\rho_{yy}}}{\sqrt{(\rho_{xx}x^2 + 2\rho_{xz}xz + \rho_{zz}z^2)/\rho_{yy} + y^2}} = \frac{C'}{\sqrt{a + y^2}}, \tag{A2}$$

where $C' = C/\sqrt{\rho_{yy}}$ and

$$a = \frac{1}{\rho_{yy}}(\rho_{xx}x^2 + 2\rho_{xz}xz + \rho_{zz}z^2) = \frac{1}{\rho_{yy}}(x, z)\begin{pmatrix} \rho_{xx} & \rho_{xz} \\ \rho_{xz} & \rho_{zz} \end{pmatrix}\begin{pmatrix} x \\ z \end{pmatrix}. \tag{A3}$$

Due to the positive definite nature of the resistivity matrix $\boldsymbol{\rho}$, the quantity $a > 0$ must be positive. According to the Fourier cosine transform

$$\int_0^\infty \frac{\cos(k_y y)}{\sqrt{a + y^2}} \mathrm{d}y = K_0(k_y\sqrt{a}), \tag{A4}$$

the transformed Green's function may be calculated by

$$\tilde{G} = C' K_0(k_y\sqrt{a}). \tag{A5}$$

Differentiating the above with respect to (x, z) and replacing $C' = \tilde{G}/K_0(k_y\sqrt{a})$ we have the gradient

$$\nabla\tilde{G} = \left[\frac{-K_1(k_y\sqrt{a})k_y}{2\sqrt{a}K_0(k_y\sqrt{a})}\nabla a\right]\tilde{G}. \tag{A6}$$

Here, ∇a can be calculated from eq. (A3). Therefore, the coefficient ν for the mixed boundary condition is obtained as follows.

$$\nu = \frac{K_1(k_y\sqrt{a})k_y}{2\sqrt{a}K_0(k_y\sqrt{a})}(\boldsymbol{\sigma} \cdot \nabla a) \cdot \mathbf{n}. \tag{A7}$$

In a 3-D case we may directly calculate the following product with eq. (A1):

$$(\boldsymbol{\sigma} \cdot \nabla G) \cdot \mathbf{n} = \left[\frac{-1}{2B}(\boldsymbol{\sigma} \cdot \nabla B) \cdot \mathbf{n}\right] G, \tag{A8}$$

where

$$B = \mathbf{r}^T \cdot \boldsymbol{\rho} \cdot \mathbf{r}, \quad \nabla B = 2 \cdot \boldsymbol{\rho} \cdot \mathbf{r}, \tag{A9}$$

From eq. (A8), the coefficient is

$$v = \frac{1}{2B}(\boldsymbol{\sigma} \cdot \nabla B) \cdot \mathbf{n}. \tag{A10}$$

APPENDIX B: THE CONDUCTIVITY TENSOR

The most general anisotropic model has six independent components of the conductivity tensor, which may be expressed by three principal values ($\sigma_{x'x'}, \sigma_{y'y'}, \sigma_{z'z'}$) and three unit eigenvectors $\mathbf{e}_i = (n_{ix}, n_{iy}, n_{iz})(i = x', y', z')$:

$$\sigma_{ij} = \sigma_{i'j'} n_{i'i} n_{j'j} = \sigma_{x'x'} n_{x'i} n_{x'j} + \sigma_{y'y'} n_{y'i} n_{y'j} + \sigma_{z'z'} n_{z'i} n_{z'j}. \tag{B1}$$

A more common anisotropic model in electrical geophysics is that defined by five parameters: $m_v \in \{\sigma_{x'x'}, \sigma_{y'y'}, \sigma_{z'z'}, \theta_0, \varphi_0\}$, where the first two eigenvalues (principal values) lie in the plane, having its unit normal given by the polar angles θ_0, φ_0, and the third eigenvalue $\sigma_{z'z'}$ is the transverse conductivity in this direction. Assuming that the x' axis has the same azimuth as the z', axis we can compute the unit vectors specifying the three perpendicular axes which define the natural rock frame as follows: $\mathbf{e}_{x'} = (\cos\theta_0 \cos\varphi_0, \cos\theta_0 \sin\varphi_0, -\sin\theta_0)$, $\mathbf{e}_{y'} = (-\sin\varphi_0, \cos\varphi_0, 0)$ and $\mathbf{e}_{z'} = (\sin\theta_0 \cos\varphi_0, \sin\theta_0 \sin\varphi_0, \cos\theta_0)$. The special case of a tilted transversely isotropic (TTI) solid has the two eigenvalues within the symmetry plane (or plane of isotropy) equal to each other $\sigma_{x'x'} = \sigma_{y'y'} = \sigma_l$ (longitudinal conductivity) and $\sigma_{z'z'} = \sigma_t$(transverse conductivity). Therefore, there are only four parameters required to characterize this popular and widely encountered class of anisotropy. Returning to the more general five parameter class of anisotropy with three distinct eigenvalues we have

$$\mathbf{n} = \begin{pmatrix} n_{x'x} & n_{x'y} & n_{x'z} \\ n_{y'x} & n_{y'y} & n_{y'z} \\ n_{z'x} & n_{z'y} & n_{z'z} \end{pmatrix} = \begin{pmatrix} \cos\theta_0 \cos\varphi_0 & \cos\theta_0 \sin\varphi_0 & -\sin\theta_0 \\ -\sin\varphi_0 & \cos\varphi_0 & 0 \\ \sin\theta_0 \cos\varphi_0 & \sin\theta_0 \sin\varphi_0 & \cos\theta_0 \end{pmatrix}, \tag{B2}$$

which yields the following six components of the conductivity tensor for 3-D modelling due to its symmetric property $\sigma_{ij} = \sigma_{ji}$.

$$\begin{pmatrix} \sigma_{xx} \\ \sigma_{xy} \\ \sigma_{xz} \\ \sigma_{yy} \\ \sigma_{yz} \\ \sigma_{zz} \end{pmatrix} = \begin{pmatrix} (\sigma_{x'x'} \cos^2\theta_0 + \sigma_{z'z'} \sin^2\theta_0) \cos^2\varphi_0 + \sigma_{y'y'} \sin^2\varphi_0 \\ (\sigma_{x'x'} \cos^2\theta_0 - \sigma_{y'y'} + \sigma_{z'z'} \sin^2\theta_0) \sin\varphi_0 \cos\varphi_0 \\ (\sigma_{z'z'} - \sigma_{x'x'}) \cos\varphi_0 \sin\theta_0 \cos\theta_0 \\ (\sigma_{x'x'} \cos^2\theta_0 + \sigma_{z'z'} \sin^2\theta_0) \sin^2\varphi_0 + \sigma_{y'y'} \cos^2\varphi_0 \\ (\sigma_{z'z'} - \sigma_{x'x'}) \sin\varphi_0 \sin\theta_0 \cos\theta_0 \\ \sigma_{x'x'} \sin^2\theta_0 + \sigma_{z'z'} \cos^2\theta_0 \end{pmatrix}. \tag{B3}$$

In a 2.5-D case, the strike direction of the geological structure is perpendicular to the surveying line, which means $\varphi_0 = 0$ in eq. (B3). Therefore, we have the following components of the conductivity tensor:

$$\begin{pmatrix} \sigma_{xx} \\ \sigma_{xz} \\ \sigma_{yy} \\ \sigma_{zz} \end{pmatrix} = \begin{pmatrix} \sigma_{x'x'} \cos^2\theta_0 + \sigma_{z'z'} \sin^2\theta_0 \\ 0.5(-\sigma_{x'x'} + \sigma_{z'z'}) \sin 2\theta_0 \\ \sigma_{y'y'} \\ \sigma_{x'x'} \sin^2\theta_0 + \sigma_{z'z'} \cos^2\theta_0 \end{pmatrix}. \tag{B4}$$